POLITECNICO DI TORINO

Corso di Laurea in Ingegneria Aerospaziale

Master's Degree Thesis

Modeling of Contact Tangential Stiffness in Dovetail Joint

Supervisor
Prof. Daniele Botto

Candidate
Lucio Costantini

March 2018

Acknowledgements

At first, I would like to express my gratitude to my parents, who sustained me economically and helped me every time I was upset, sad and downhearted. I would never end my university journey without them.
Then, I wish to thank Prof. Daniele Botto for his help and advices and his guidance though numerical and analytical handling of my work.
Naturally, I must thank my brothers and sisters, Elisabetta, Maria, Mario and Marco for continuing supporting me despite the distance from home.
I also wish to thank all my dear friends, coming from many regions of Italy, who never stopped encouraging me, making me laugh and sharing their hopes with me.
Finally, I would like to thank my girlfriend Beatrice, but I think that all the words I know would never be sufficient.

Abstract

The typical contact between rotor disc and blade dovetail characterizes itself for being not merely normal, but also tangential, because of the complex load system applied to the blade. This fact has a great impact from the Fretting Fatigue point of view, because unexpected oscillating shear loads can lead to premature failures and service mishaps in gas turbine engines. In this work an analytical model is proposed to determine the tangential contact stiffness, assuming constant pre applied normal load and increasing tangential load. The system geometry is simplified and reduced to a bi-dimensional punch in contact with a flat body, accordingly with analytical theories found in literature. These models allow to find both normal and tangential contact pressures, while the tri-dimensional Cerruti potential theory is employed to obtain the hysteresis loop, and the tangential contact stiffness. Finally, the analytical results are compared with numerical calculations elaborated with a bi-dimensional FE model.

Contents

Chapter 1

Introduction

When contact occurs between two bodies, a stiffness relationship must be established. This relationship is represented schematically through an elastic spring, put between the two bodies, having its own stiffness, called *contact stiffness*. The force generated by the contact will be then the product between the contact stiffness and the penetration. In the ideal case with rigid bodies, there should be no penetration, even with non zero load, and the contact stiffness should be infinite. Modeling the contact stiffness is fundamental, because it expresses the relationship between load and displacements, meaning that it is possible to determine the contact force knowing the penetration and vice versa.
From many references in literature, it is known that the first who found a closed-form solution for static, frictionless and elastic contact was Hertz, under the assumption of elliptical contact area and small contact surface (length and width small compared to curvature radii of bodies in contact). However, from Ref.[1], analytical solutions for contact problems with Coulomb friction hypothesis and both normal and tangential loads were found only for a restricted number of contact geometries, such as elastic spheres [2], homogeneous, isotropic elastic bodies [3] and flat punch with rounded edges from Ref.[1, 5, 6].
The last one is mostly important, because it allows to study in relatively simple way the contact problem between blade dovetail joint and rotor disc in gas turbine engines.

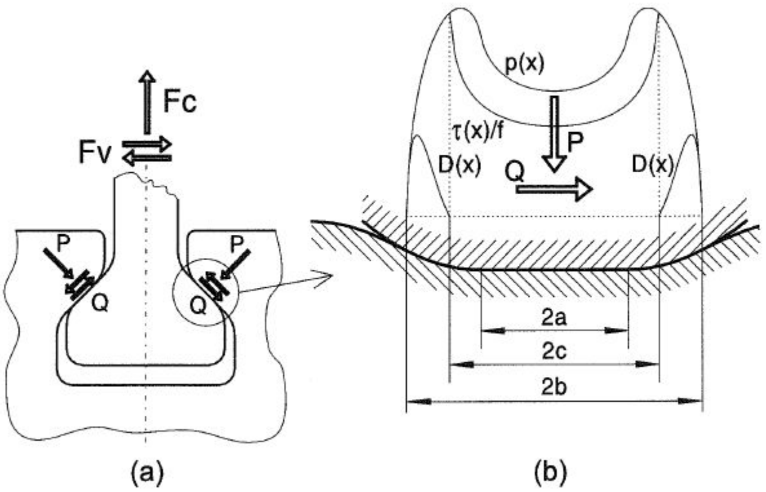

Figure 1.1: Dovetail joint and disc schematics (a) and flat punch model (b) from Ref.[4].

As pointed out in Ref.[4] and shown in figure 1.1, the blade itself is loaded in normal conditions not only with a centrifugal force F_c, but also with an oscillating force normal to blade axis. As result, the dovetail joint is subjected to a normal load P, that will be considered constant, and a tangential load Q, that will be variable.
The aim of this work is to verify the analytical model of tangential contact stiffness, showed in Ref.[6], by confronting its results with those obtained with a FE model, that will be introduced in following chapters. This is important, because alternating tangential contact pressure under normal load leads to small tangential motion between bodies in contact is the cause of fretting fatigue (FF) in dovetail joints. Referring to USAF data in Ref.[4], FF "is responsible for about one out of six in service 'mishaps' in gas turbine engines for which high cycle fatigue (HCF) is itself the largest single cause of failure. These two facts combine to give a clear idea of the relevance of the phenomenon for such safety-critical applications. Despite the remarkable progress, FF is still one of the most 'inexact' areas of figure, where effort is now being focused".
It should be clear now the importance of studying tangential contact problems, in terms of engine safety, maintenance costs and mechanical design of contact elements in gas turbine engines. However, much work has been done in recent times (see Ref.[1, 5, 6]) in terms of development of bi-dimensional analytical models and confront with FEM results, but mainly regarding the stress and deformation state. In following chapters, the most common analytical model for this problem in literature will be presented, then the contact hysteresis loop will be created, starting from tangential contact pressure. Being then, in infinitesimal terms, the contact stiffness defined as the derivative of tangential load with respect to relative displacement, the final result can be easily obtained by the virgin curve of hysteresis loop.
The mentioned model allows to verify the effects of main contact parameters (geometry, materials and applied loads) on the final solutions and is based on following steps [6]:

- The friction contact, represented in figure 1.2 is simulated by a 3D flat indenter pressed against an infinite half-plane.
- The normal and tangential pressures of a bi-dimensional punch over an infinite half-plane are calculated by means of theory explained in Ref.[5].
- The 2D solution will be extended to 3D, assuming that it will not vary along the axis of the indenter.
- A solution is find for different values of tangential pressure, monotonically increasing, in order to build the tangential load vs relative displacement curve, i.e. the virgin curve.
- The Masing rule from Ref.[8] is applied to obtain the complete micro-slip hysteresis cycle.

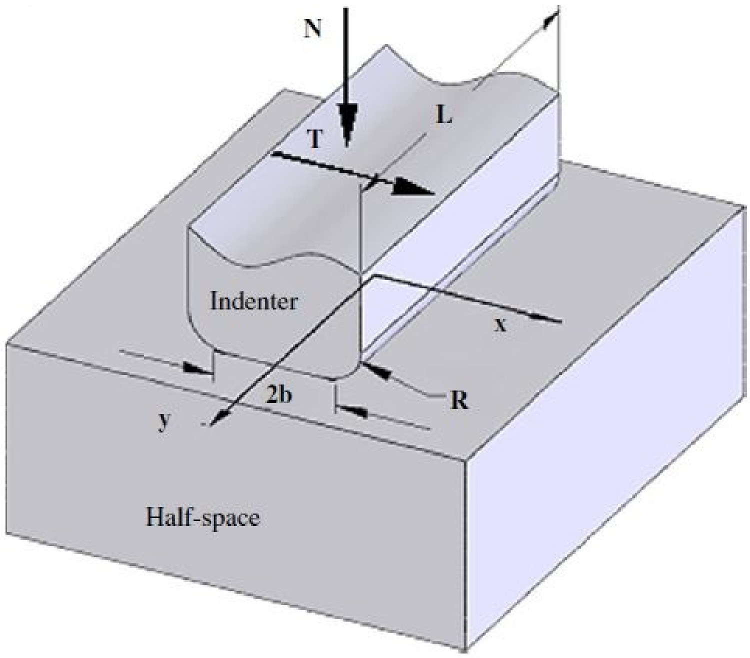

Figure 1.2: Tri-dimensional model of the indenter from Ref.[6].

Chapter 2

Normal Pressure

2.1 Preliminary hypotheses

The general assumptions adopted in literature for the normal contact problem are the followings:

1. Isotropic and perfectly elastic materials.
2. Bodies' half planes in contact are elastically similar.
3. Surface roughness is neglected, so that contact surfaces are considered perfectly smooth.
4. The Coulomb friction law is used and friction coefficient μ is known and constant.
5. The normal and tangential contact problems are assumed uncoupled, in order to simplify the construction of hysteresis curves.

2.2 Punch geometry definition

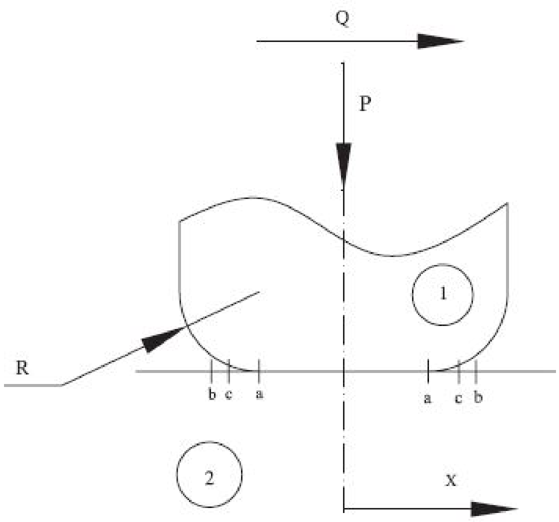

Figure 2.1: Bi-dimensional punch geometry from Ref.[6].

In figure 2.1 the main geometric properties of the elastic punch are displayed with previously described load system. Considering the punch lying in x-y plane, it is defined by the following parameters:

- Half-width of the flat part: a.
- Half-width of the contact area: b.
- Half-width of the central stick area: c.
- Radius of curvature: R.
- Normal load per unit length: P.
- Tangential load per unit length: Q.

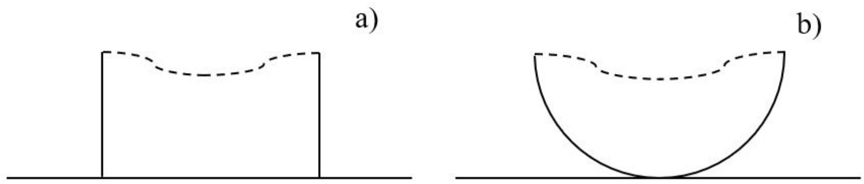

Figure 2.2: Flat-end punch (a) vs Hertzian indenter (b).

This particular geometry, simplified representation of the dovetail joint, can be also considered as midway between two known contact geometries, showed in figure 2.2, i.e. the flat-end punch and the Hertizan indenter. A very common parameter used to describe these geometries is the ratio between flat part half-width and radius of curvature, a/R. In flat-end punch a/R tends to infinity, being the shape almost rectangular, and in Hertzian indenter the spheric shape causes the ratio to fall to zero. It can be easily understood that intermediate values of a/R generate every type of rounded-end punch, each one with a different solution at the same load conditions as will be shown in following sections.
The values of geometric parameters chosen for this problem are $a = 1.5\ mm$ and $R = 0.5\ mm$, representatives of the real physical dimensions.

2.3 Problem formulation

While analytical solutions do not exist for the 3D problem [6], a closed-form 2D one has been provided in Ref.[5], under the assumption that both contact bodies have the same elastic constant. In this way, the profile of the 2D punch is specified by its slope at each point, $h'(x)$. The normal and shear traction distributions over the contact area, $p(x)$ and $q(x)$, can be found by solving the integral equation

$$\frac{E^*}{2}h'(x) = \frac{1}{\pi}\int_L \frac{p(\xi)d\xi}{x-\xi} - \beta q(\xi) \tag{2.1}$$

where E^* is a measure of composite stiffness of the bodies, defined under plane strain conditions by

$$\frac{1}{E^*} = \frac{1}{E_1}(1-\nu_1^2) + \frac{1}{E_2}(1-\nu_2^2) \tag{2.2}$$

The detailed development of this theory can be found in Ref.[5] and exceeds the aim of this work. Once the integral equation 2.1 is solved, the results inside the contact region $-b \le x \le b$ can be obtained in terms of non-dimensional length using

$$x = a\frac{\sin\phi}{\sin\phi_0} \tag{2.3}$$

The averaged non-dimensional pressure distribution results then

$$\frac{bp(\phi)}{P} = -\frac{2/\pi}{\pi - 2\phi_0 - \sin 2\phi_0}\left\{(\pi-2\phi_0)\cos\phi + \ln\left[\left|\frac{\sin(\phi+\phi_0)}{\sin(\phi-\phi_0)}\right|^{\sin\phi}\left|\tan\frac{\phi+\phi_0}{2}\tan\frac{\phi-\phi_0}{2}\right|^{\sin\phi_0}\right]\right\} \tag{2.4}$$

The angle ϕ_0 implicitly specifies the contact half-width b and can be found as function of normal load P from overall equilibrium:

$$\frac{2PR}{a^2E^*} = \frac{\pi - 2\phi_0}{4\sin^2\phi_0} - \frac{\cot\phi_0}{2} \tag{2.5}$$

It can be noted that ϕ_0, and so the contact length, is function of both geometry (a, R), materials (E^*) and load P. The non-dimensional pressure obtained with equation 2.4 is plotted in region $-\pi/2 \le \phi \le \pi/2$, corresponding to $-b \le x \le b$. The two sets are bond by the relationships

$$\sin\phi = \frac{x}{b} \quad ; \quad \sin\phi_0 = \frac{a}{b} \tag{2.6}$$

that allow to find results in dimensional form.

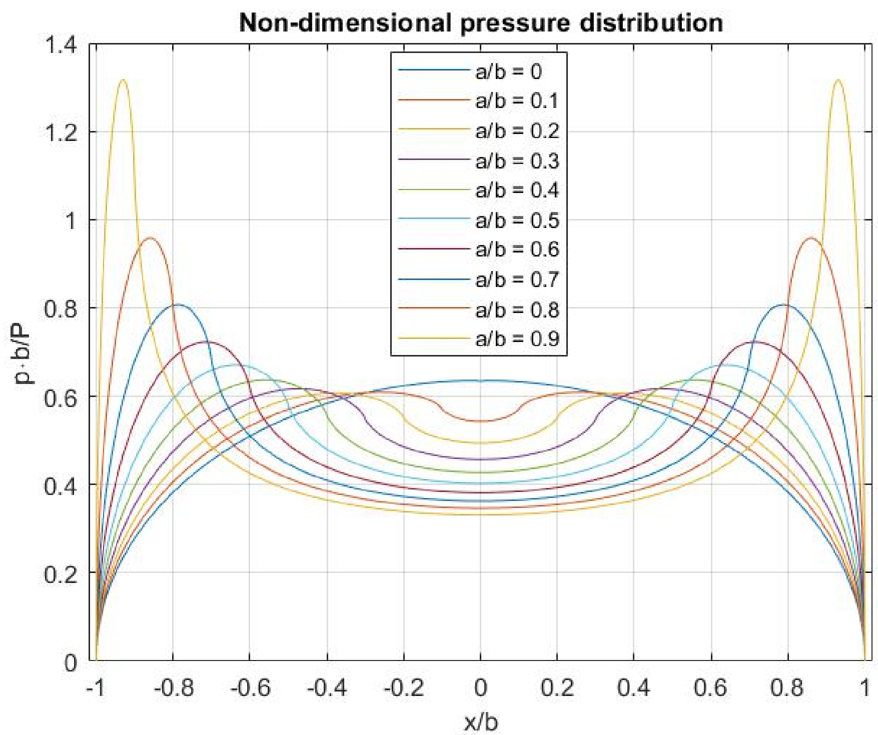

Figure 2.3: Non-dimensional pressure for multiple geometries.

Being the equation 2.5 transcendental, once specified the known parameters it can be solved numerically. Its output, ϕ_0, is then used as an input for equation 2.4.
Figure 2.3 shows non-dimensional pressure plotted against the non-dimensional contact length (i.e $-1 \leq \sin\phi = x/b \leq 1$) for different values of ratio a/b. This geometric parameter is related to a/R, because it changes as the punch shape tends to an Hertzian indenter ($a/b \to 0$) ot to a flat-end punch ($a/b \to 1$), but in both cases the stress must vanish at the edge of contact area, i.e. $x = b$. For an Hertzian indenter, the contact area is very small and tends to one point at the limit case $a = 0$, so the pressure distribution has parabolic shape, with the maximum coincident to the original contact point.
As a/b increases, the flat part of the punch becomes larger and tends to uniform the pressure at the center of contact zone. An interpretation of this phenomenon can be found by creating an analogy between the rounded edge of the punch and the notch effect (a discontinuity in the shape of a component leads to a stress accumulation). As for a notch, the fillet of a punch represents a discontinuity in the profile and, as showed in figure 2.3, causes the presence of two symmetric spikes of stress, increasing in magnitude as the shape tends to a flat-end punch, inside the rounded portion of the punch. This time, the limit case is the flat-end punch, where the fillet disappear and the discontinuity becomes normal to the flat surface. In theory, as a equals b, the pressure spikes should go to infinite, according to classical formulations. That obviously does not happen in reality, but, when $a = b$, the equation 2.4 has a singularity, so that it cannot be displayed in figure 2.3.

2.4 Dimensional results

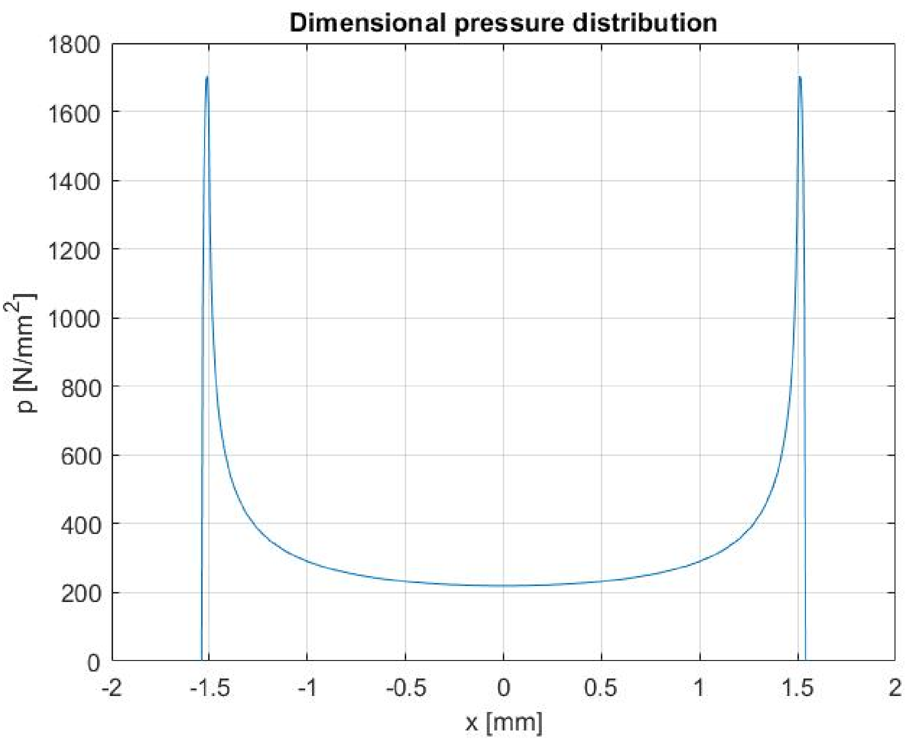

Figure 2.4: Dimensional contact pressure for defined geometry.

In order to find the contact pressure distribution for previously defined geometry, the equation 2.5 must be numerically solved. The inputs are the yet defined geometric parameters ($a = 1.5\,mm$ and $R = 0.5\,mm$), the normal load per unit length $P = 1050\,N/mm$ (corresponding to a pressure of $262.5\,N/mm^2$ applied on the top surface of the punch), that is equal to the total load N divided by the contact length L and the composite stiffness E^*. The elastic constants of the 2 bodies in contact must be the same, because of the 2D assumption, and the value of $E_1 = E_2 = 2 \cdot 10^5\ N/mm^2$ has been chosen. Using that value as input for the equation 2.2, the corresponding composite stiffness results $E^* = 1.0989 \cdot 10^5\,N/mm^2$.
Solving then the equation 2.5, the output is $\phi_0 = 1.3406\,rad$ and the half-width of the contact area can be easily determined by

$$b = \frac{a}{\sin \phi_0} = 1.5407\,mm \tag{2.7}$$

Comparing what found with the pressure curves in figure 2.3, the geometric ratios in this problem, $a/b = 0.9736$ and $a/R = 3$, indicate that the shape of the punch is closer to a flat-end punch than to an Hertizan indenter. Indeed, the dimensional contact pressure plotted in figure 2.4 has 2 spikes at the very edge of the contact area, which magnitude is more than eight times higher than the almost constant one in the center of the flat part of the punch. This fact is very important from static point of view, because the normal stress could exceed the yield limit of the material and lead to unexpected plastic deformations in the rounded part of the punch.
The results of this chapter will be used in the following one as starting point to determine the shear contact stress for variable tangential load, while the normal load will be kept constant, as widely accepted in reference literature.

Chapter 3

Shear Traction

3.1 Introduction

Carrying on with the theory exposed in Ref.[4], under the assumptions of steady normal load and monotonically increasing tangential force, the contact shear traction distribution will be determined in this section.
Because of the assumption of the Coulomb friction law, knowing the normal load $P = 1050\, N/mm$, the maximum tangential load applicable to the top surface of the punch is

$$Q_{max} = \mu \cdot P = 525\, N/mm \tag{3.1}$$

being the friction coefficient $\mu = 0.5$.
If a tangential load of $Q = Q_{max}$ is applied, the friction reaction force can not resist anymore to the external load, so the punch would detach from the flat surface and slide along the direction imposed by Q. Moreover, even if $Q < Q_{max}$ the points in contact do not remain stuck, but begin to slowly slide from the initial position. This phenomenon is known as microslip.
For low values of Q, microslips occur at the edges of contact region [6], where the stress is higher (i.e. $c \leq |x| \leq b$), being c the half-width of contact zone. As $Q/\mu P$ approaches the unity, c tends to move towards the center of the contact area, the last point that remains stuck, because of the spreading of the microslips from the edges. In the end, when $Q/\mu P = 1$, the entire contact surface begins to slip and gross slip occurs.

3.2 Problem formulation

In order to determine the boundary between stick and slip zones, i.e. c, a second integral equation is needed with respect to the normal load case, which relates the displacements of contact points with surface shear traction

$$\frac{E^*}{2} g'(x) = \frac{1}{\pi} \int_L \frac{q(\xi) d\xi}{x - \xi} + \beta p(\xi) \tag{3.2}$$

where $g(x)$ is the relative displacement of the surface particles.
Tangential equilibrium will be then satisfied by

$$Q = \int_L q(\xi) d\xi \tag{3.3}$$

The value of the half-width of contact zone c can be determined from the following considerations:

- Within the stick zone, the relative tangential displacement must be zero, so that

$$g'(x) = 0 \quad \text{for } -c < x < c \tag{3.4}$$

- The contact tangential pressure must not exceed the maximum value, i.e.

$$|q(x)| < \mu p(x) \quad \text{for } -c < x < c \tag{3.5}$$

- In the slip zones the shearing traction can not overcome the friction reaction, that is

$$q(x) = \mu p(x) \quad \text{for} \quad \begin{cases} -b < x < -c \\ c < x < b \end{cases} \tag{3.6}$$

- From energetic considerations, the shear traction must always oppose the direction of change of the slip direction, i.e.

$$\text{sgn}[q(x)] = \text{sgn}\left(\frac{\partial q}{\partial t}\right) \tag{3.7}$$

In order to find a solution for the equation 3.2, the two situations of $c < b$ and $c > b$ must be analyzed separately.
In the first case, as previously said, microslips do not occur inside the contact stick zone, so relative displacements $g(x)$ and its derivatives can not exist. Adding this condition at the equation 3.2, it is found that

$$\frac{E^*}{2} g'(x) = 0 = \frac{1}{\pi} \int_L \frac{\mu p(\xi) + q^*(\xi) d\xi}{x - \xi} = \frac{1}{\pi} \int_{L_{stick}} \frac{q^*(\xi) d\xi}{x - \xi} \tag{3.8}$$

The tangential pressure that will be obtained is the result of the superposition of the full sliding one with a 'difference' part $q^*(x)$, which is a perturbation within the stick zone.
Taking now in consideration the case where the stick zone extends into the rounded part of the flat ($c > b$), the resulting shearing traction can be found by solving the following integral equation:

$$\frac{1}{\pi} \int_{L_{stick}} \frac{q^*(\xi) d\xi}{x - \xi} = -\frac{\mu E^*}{2} \begin{cases} -(a + x)/R & \text{for} \quad -c \leq x \leq -a \\ 0 & \text{for} \quad -a \leq x \leq a \\ -(x - a)/R & \text{for} \quad a \leq x \leq c \end{cases} \tag{3.9}$$

It can be found that the same integral equation describing the case of normal loading can be applied to obtain the corrective shearing traction $q^*(x)$. This means that the results found in chapter 2 can be used to determine $q^*(x)$, after changing the relative parameters.
Then, in simple terms, the shear traction depends on the normal pressure, the corrective term and the friction coefficient, and assumes the following expression:

$$q(x) = \mu p(x) - q^*(x) \tag{3.10}$$

The problem is so reduced to the calculation of $q^*(x)$, which expression is very similar to the one found for $p(x)$.

$$\frac{cq^*(\vartheta)}{\mu P - Q} = -\frac{2/\pi}{\pi - 2\vartheta_0 - \sin 2\vartheta_0} \left\{ (\pi - 2\vartheta_0) \cos \vartheta_0 + \ln \left[\left| \frac{\sin(\vartheta + \vartheta_0)}{\sin(\vartheta - \vartheta_0)} \right|^{\sin \vartheta} \left| \tan \frac{\vartheta + \vartheta_0}{2} \tan \frac{\vartheta - \vartheta_0}{2} \right|^{\sin \vartheta_0} \right] \right\} \tag{3.11}$$

The auxiliary angle ϑ is used to recreate the non-dimensional length set, while the parameter ϑ_0 is determined by numerically solving the following equation

$$\frac{4PR}{a^2 E^*} \left(1 - \frac{Q}{\mu P}\right) = \frac{\pi - 2\vartheta_0}{2 \sin^2 \vartheta_0} - \cot \vartheta_0 \tag{3.12}$$

where

$$\sin \vartheta_0 = \frac{a}{c} \tag{3.13}$$

The procedure for resolving the equation 3.11 and obtain $q^*(x)$ is the same described in chapter 2 for normal load.

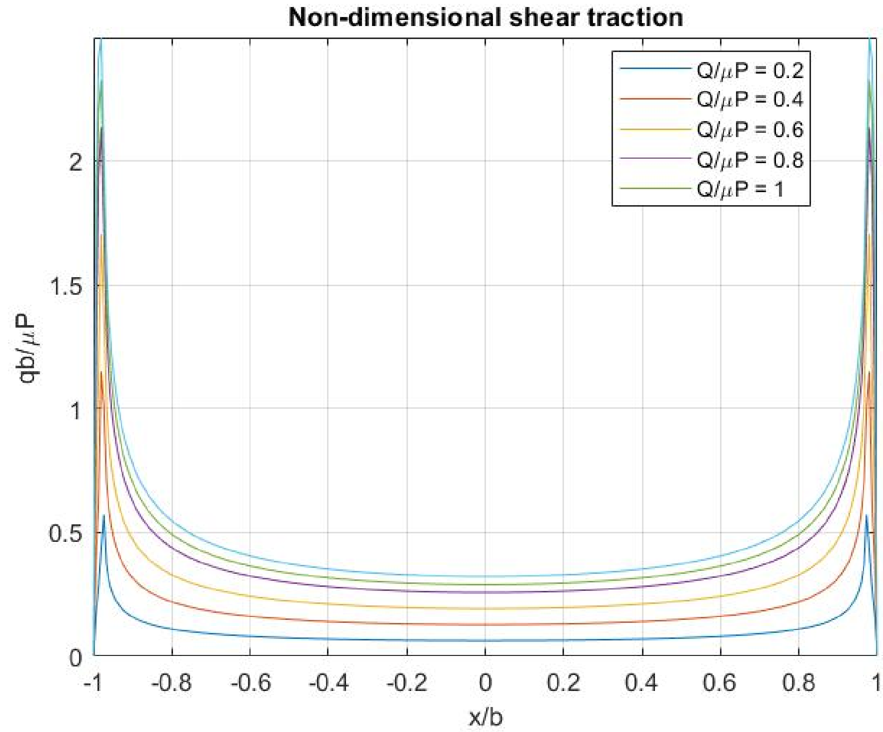

Figure 3.1: Non-dimensional contact shearing traction for varying tangential load.

Non-dimensional curves of shearing traction for different values of tangential load Q are showed in figure 3.1. The fact that these curves derive directly from the normal pressure curve explains the similar shapes, with almost-constant pressure central stick zone and the two symmetric spikes. The same considerations made for normal pressure can be hen applied to this case.
It looks interesting to evaluate the relationship between the non-dimensional tangential load $Q/\mu P$ and the non-dimensional stick zone size c/b. From Ref.[5] the following relationship is given

$$\frac{|Q|}{\mu P} = 1 - \left(\frac{c}{b}\right)^2 \frac{\pi - 2\vartheta_0 - \sin 2\vartheta_0}{\pi - 2\phi_0 - \sin 2\phi_0} \qquad \text{for} \quad c > a \tag{3.14}$$

In figure 3.2 is the relationship between the non-dimensional shearing load and the stick zone size for different geometries. For $a/b = 0$ the Cattaneo-Mindlin solution for the Hertzian geometry is found. As a/b increases, there is a smooth transition towards the flat-end punch shape. It can be noted that the slip/slide transition occurs when all the rounded part of the contact is enveloped into the slip zone, i.e. $a/b = c/b$.

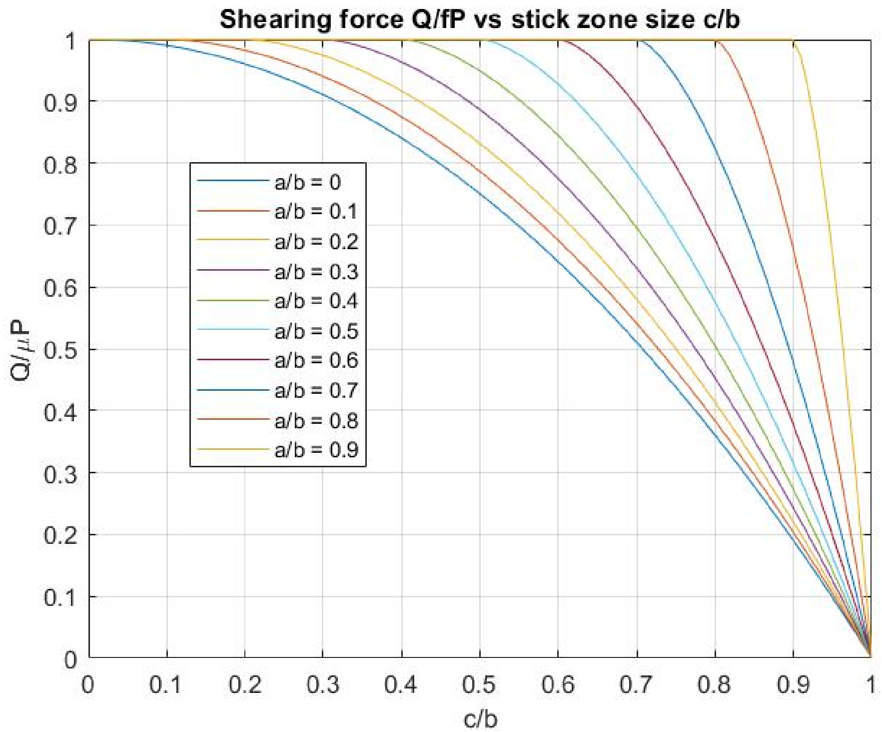

Figure 3.2: Non-dimensional shearing force vs stick zone size.

3.3 Dimensional results

As previously done, passing from the non-dimensional form of shearing traction showed in the equation 3.11 to the dimensional curves, plotted in figure 3.3 is relatively straightforward. Knowing that this model always predicts microslips at the edges of contact area, even with low tangential loads, the pressure spikes can reach half of the magnitude of normal pressure spikes. This is very important form the FF point of view, because the variable shearing traction at the edges can be eight times the value relative to the central stick zone.
After numerically solving the equation 3.12, the auxiliary angle θ_0 can be determined, so it is possible to calculate the half-width of the central stick area by means of

$$c = \frac{a}{\sin \theta_0} \tag{3.15}$$

Obviously, each value of c is evaluated for the corresponding input of tangential load Q. Referring to figure 3.2, after fixing the desired geometry (i.e the ratio a/b) the half-width of the central stick zone will follow the chosen curve for variable Q.

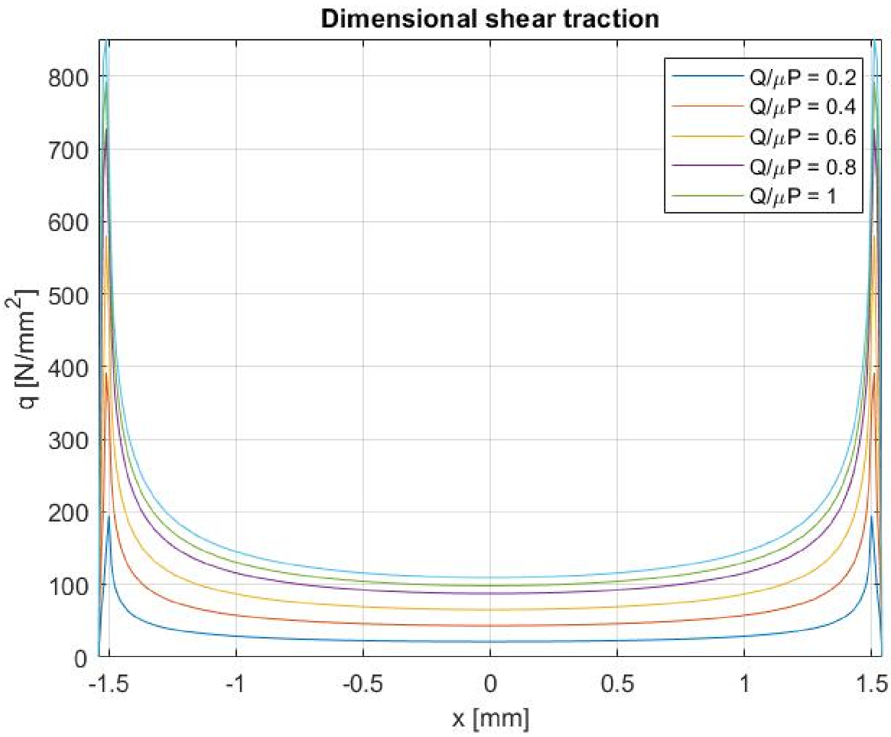

Figure 3.3: Dimensional shearing traction for varying tangential load.

Chapter 4

Hysteresis Loop

4.1 Formulation of the relative displacement

The bi-dimensional results found in previous chapters are very useful, in order to evaluate stresses, strains and fretting fatigue for this kind of contact. However, these are not sufficient if the calculation of hysteresis curves and tangential contact stiffnesses is requested. For this reason, following the theory explained in Ref.[6], the 2D assumption vanishes and the classical approach of surface traction distributed upon a half-space is adopted.

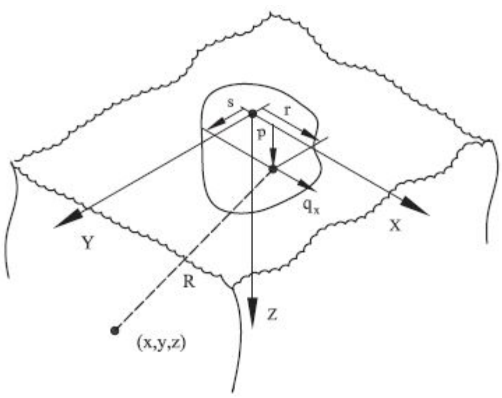

Figure 4.1: A half-space subject to the surface traction elements p and q_x, located at (r, s), and a general point (x, y, z), where the potential must be evaluated, from Ref.[6].

In order to obtain a relationship between tangential force and relative displacement, it is useful to recall the potential theory developed by Cerruti and Bussinesq [7], that provides a set of equations relating the displacement field to the shear traction distribution. Then, for an half-space subject to the only shear traction distribution q_x, the displacements set resulting is

$$u_x = \frac{1+\nu}{2\pi E} \int\int q_x(r,s) \left[\frac{1}{R} + \frac{1-2\nu}{R+z} + \frac{(r-x)^2}{R^3} - \frac{(1-2\nu)(r-x)^2}{R(R+z)^2} \right] drds \tag{4.1}$$

$$u_y = \frac{1+\nu}{2\pi E} \int\int q_x(r,s) \left[\frac{(r-x)(s-y)}{R^3} - \frac{(1-2\nu)(r-x)(s-y)}{R(R+z)^2} \right] drds \tag{4.2}$$

$$u_z = -\frac{1+\nu}{2\pi E} \int\int q_x(r,s) \left[\frac{(r-x)z}{R^3} + (1-2\nu)\frac{(r-x)}{R(R+z)} \right] drds \tag{4.3}$$

where

$$R^2 = (x-r)^2 + (y-s)^2 + z^2 \tag{4.4}$$

as showed in figure 4.1.
The contact is supposed to be 1D, so only the u_x displacement will be considered. According to Ref.[6] and previous literature, being the center of contact the last point to remain stuck, u_x should be evaluated in $x = y = z = 0$. Substituting these conditions into the equation 4.1, it is found that

$$u_x = \frac{1+\nu}{2\pi E} \int\int q_x(r,s) \left[\frac{2-2\nu}{R} + \frac{2\nu r^2}{R^3}\right] drds \tag{4.5}$$

Assuming that the shear traction $q(x)$, evaluated in previous chapter, is constant along the indenter length L, the equation 4.5 becomes

$$u_x = \frac{1+\nu}{2\pi E} \int_{-b}^{b} q_x(r,s) \int_{-L/2}^{L/2} \left[\frac{1-\nu}{\sqrt{r^2+s^2}} + \frac{\nu r^2}{(r^2+s^2)^{3/2}}\right] drds \tag{4.6}$$

After several mathematical passages explained in Ref.[6], the final formulation of this integral equation is

$$u_x = -\frac{2(1-\nu^2)}{\pi E} \int_{-b}^{b} q_x(r) \ln\left|\frac{r}{b}\right| dr + \frac{2(1-\nu^2)}{\pi E} \left(\ln\left|\frac{L}{b}\right| + \frac{\nu}{1-\nu}\right) \int_{-b}^{b} q_x(r)dr \tag{4.7}$$

where

$$Q = \int_{-b}^{b} q_x(r)dr \tag{4.8}$$

Finally, it is possible to evaluate the tangential relative displacement δ_x between distant points belonging to the 2 bodies in contact, by means of the following integral equation

$$\delta_x = u_{x1} - u_{x2} = \frac{2}{\pi E^*} \left[-\int_{-b}^{b} q_x(r) \ln\left|\frac{r}{b}\right| dr + Q\left(\ln\left|\frac{L}{b}\right| + \frac{\nu}{1-\nu}\right)\right] \tag{4.9}$$

4.2 Virgin curve analysis

The equation 4.9 establishes a relationship between the relative displacement δ_x and the tangential load per unit length Q. As pointed out during the introduction, Q monotonically increases from zero to the maximum value $Q_{max} = \mu P$, so that is possible to plot the so called *Virgin Curve*. Thanks to this curve, using a particular hypothesis, it is possible to mathematically recreate the whole hysteresis loop without using other curves or formulations. The non-dimensional virgin curve for defined geometry is plotted in figure 4.2. It is possible to notice that the virgin curve has an almost straight line shape, with very small variations in slope. This fact indicates that the relationship between the relative displacement and the tangential load is almost linear, i.e. easy to study and interpret. The particular non-dimensional form of the magnitudes studied has been taken from Ref.[6].
Since the fact that the 3D assumption is used, it seems interesting to evaluate how the virgin curve can vary for different values of the indenter length L. It is quite straightforward to obtain the new virgin curve, because it is sufficient to change the L value in equation 4.9, being the shear traction constant along the z axis. The results are displayed in figure 4.3. There is not a substantial change in the shape of the curves with the variation of the L/b ratio, but what changes is the slope. It clearly results that, as L/b increases, the line slope decreases in a non-linear way.

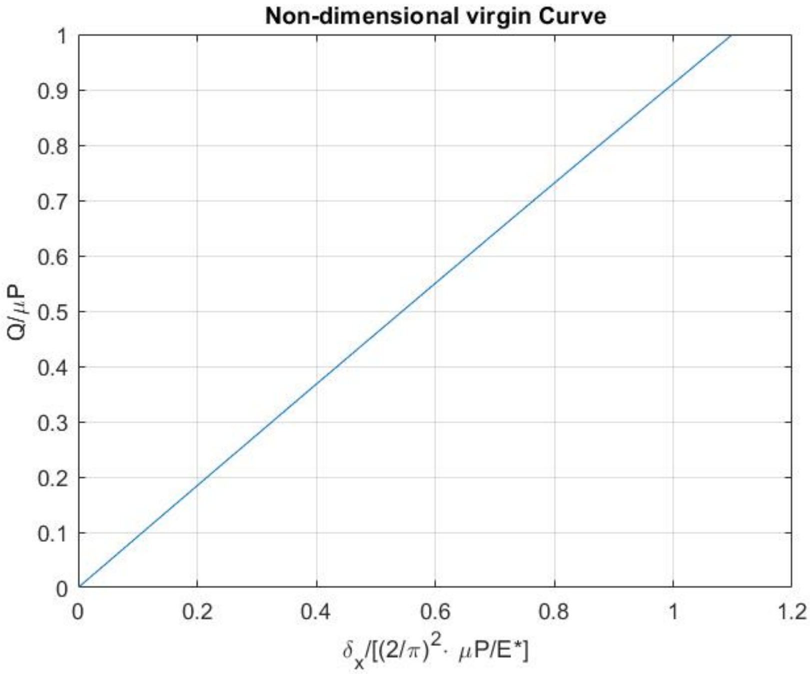

Figure 4.2: Non-dimensional virgin curve for defined geometry.

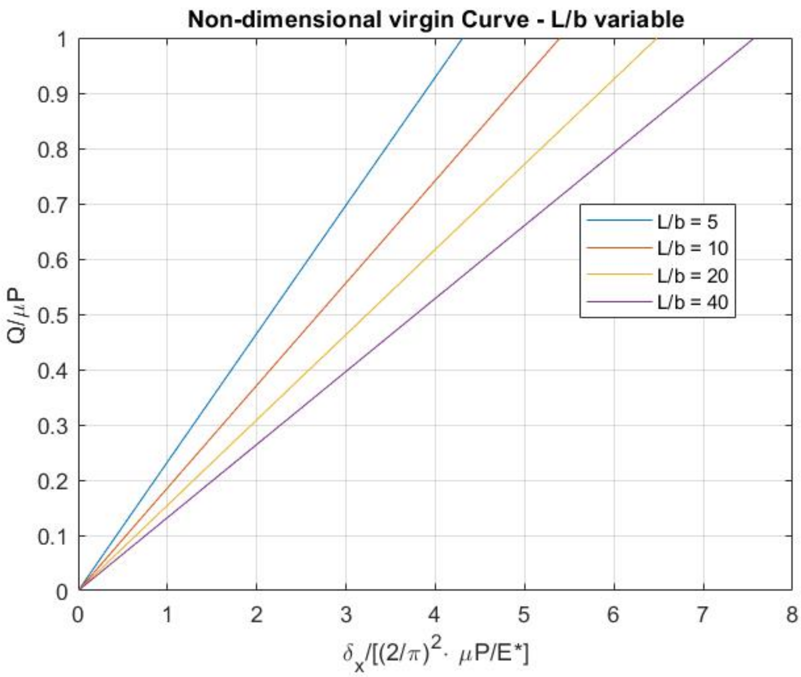

Figure 4.3: Non-dimensional virgin curve for variable indenter length.

That means that the higher the indenter length, the higher will result the relative displacement for constant tangential load, i.e. the contact seems to be less stiff for a wide indenter. It can be also demonstrated mathematically, because, from the equation 4.9 is given that

$$\delta_x \propto Q\left(\ln\left|\frac{L}{b}\right| + \frac{\nu}{1-\nu}\right) = Q\left(\ln\left|\frac{L}{b}\right| + C\right) = Q \cdot m \quad \rightarrow \quad \delta_x \propto Q \cdot m \qquad (4.10)$$

The parameter m, in this problem, depends non-linearly only on the indenter length L. Another way to explain this phenomenon is that the global tangential load applied to the 3D indenter is $T = Q \cdot L$. In this problem, the tangential load per unit length Q is kept constant, so T will increase proportionally to L, thus generating higher stresses and displacements, as demonstrated in figure 4.3.

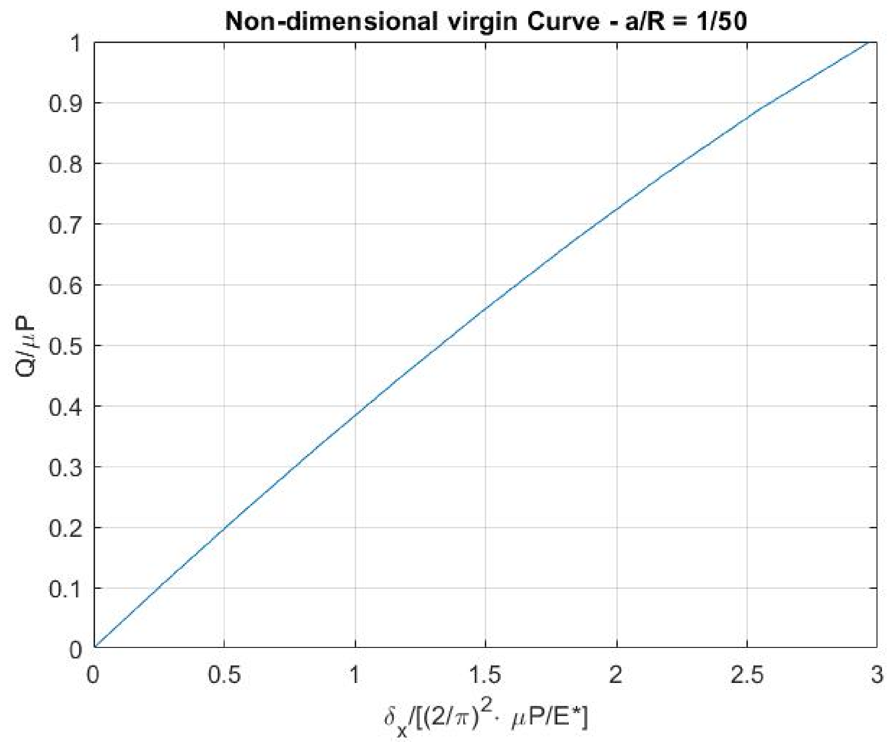

Figure 4.4: Non-dimensional virgin curve for a quasi-Hertzian shape.

Finally, the virgin curve for a quasi-Hertzian shape is plotted in figure 4.4. This example has been given in order to evaluate the difference in the $Q - \delta_x$ relationship between the study case geometry (with geometric ratio $a/R = 3$) and one close to an Hertzian indenter, with $a/R = 1/50$. It is noted that the shape of the new curve is not linear anymore, but polynomial, which slope decreases as Q grows. Then, it can be easily understood that the system geometry affects the behaviour of the contact, and so the entity of stresses, strains and finally of the contact stiffness.

4.3 Evaluation of the Hysteresis Loop

As previously stated, starting from the virgin curve, described by equation 4.9, it is possible to obtain the hysteresis loop in microslip regime, i.e. for $Q/\mu P < 1$. That is different from the gross slip regime, that takes over when the maximum tangential load is exceeded ($Q/\mu P > 1$). In this work, only the microslip regime is considered, in order to analyze the conditions under which the fretting fatigue can lead to premature failures or crack propagation. The whole hysteresis loop for microslip regime can be computed from the monotonic curve thanks to the Masing hypothesis [8]. The mathematical expression of this hypothesis is

$$\delta_u(Q) = \delta^* - 2M\left(\frac{Q^* - Q}{2}\right) \tag{4.11}$$

where δ^* is the relative displacement at the load reversal (i.e. when the tangential load is maximum) and the function M is simply the monotonic loading curve of the equation 4.9, evaluated in $(Q^* - Q)/2$, where $Q^* = Q_{max}$.
In this way, it is possible to build the unloading curve, and from that retrieve the reloading curve by means of the following relationship

$$\delta_r(Q) = -\delta_u(-Q) \tag{4.12}$$

which states that the reloading displacement δ_r is the negative of the unloading displacement with a negative argument. Obviously, there is an analogy between the hysteresis loop of an oscillating tangential load and the one related to the elasto-plastic materials. In fact, Masing models can describe the hysteretic behavior of many physical systems [8], such as material plasticity, structural dynamics and vibrations, control systems and magnetics.

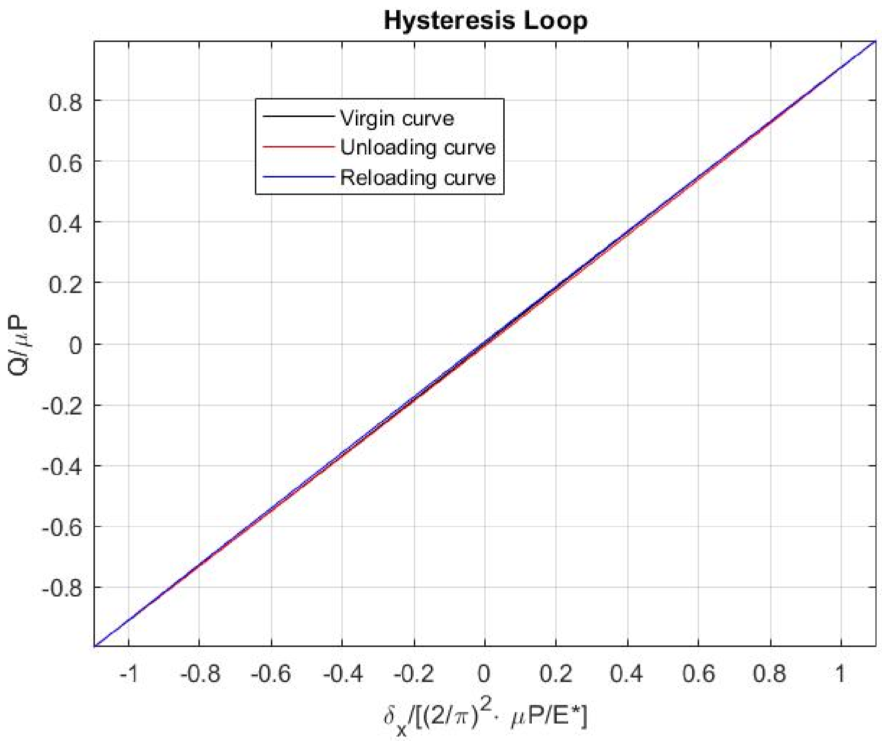

Figure 4.5: Hysteresis Loop for microslip regime using the problem's geometry.

The full hysteresis loop, build with curves described in equations 4.9, 4.11 and 4.12 is plotted in figure 4.5 for both positive and negative values of tangential load per unit length. Due to the particular geometry in study, the hysteresis loop is difficult to observe and all of the three curves are almost coincident. A zoomed plot of the hysteresis loop in the origin zone is provided in figure 4.6.

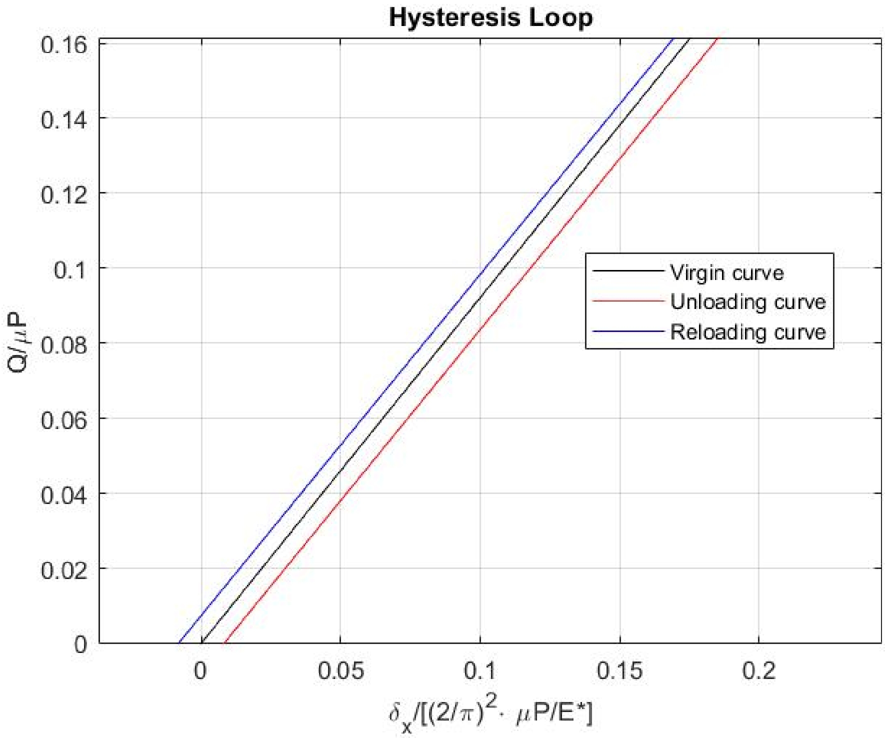

Figure 4.6: Zoomed section of the hysteresis loop.

In order to better understand the behavior of the hysteresis loop and to improve its visibility, a new loop has been calculated, based on the rounded shape geometry which virgin curve is plotted in figure 4.4, with a geometric ratio of $a/R = 1/50$, remembering that the ratio of the study case geometry is $a/R = 3$.
As expected from the equation 4.12, the reloading curve is the antisymmetric of the loading curve with respect to the x axis. Confronting that plot with the one in figure 4.5, not only the cycle is larger and the curves are well visible, but also the non-dimensional relative displacement for maximum tangential load is higher in the second case. The reason for this fact can be found by recalling the equation 4.9. Looking at the integral term of the equation, it can be stated that the relative displacement δ_x will increase if the product of the shear load $q_x(r)$ and the function $fun = \ln|r/b|$ does the same. The plot of fun has been provided in figure 4.8. This function has a negative maximum in the origin of coordinate system, i.e. at the center of the contact stick zone. It is clear that the integral will grow if the shear traction assumes high values in proximity of the origin. However, looking at figure 3.3, even for tangential loads near to the maximum, in the central contact zone the shear load is low, so the integral part of the equation 4.9 results to be negligible with respect to the linear part, highlighted in the equation 4.10.
On the contrary, for a quasi-Hertizan geometry both normal and shear tractions have low edge spikes and relatively high values for the stick zone. Thus, in this case the integral part will prevail over the linear one and the relative displacement will consequently rise.

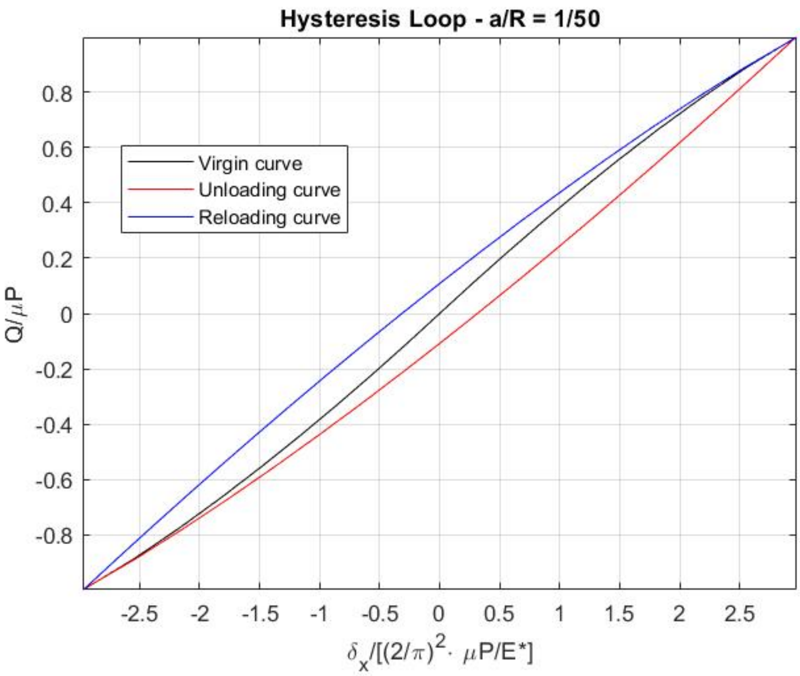

Figure 4.7: Hysteresis Loop for microslip regime using a rounded shape geometry.

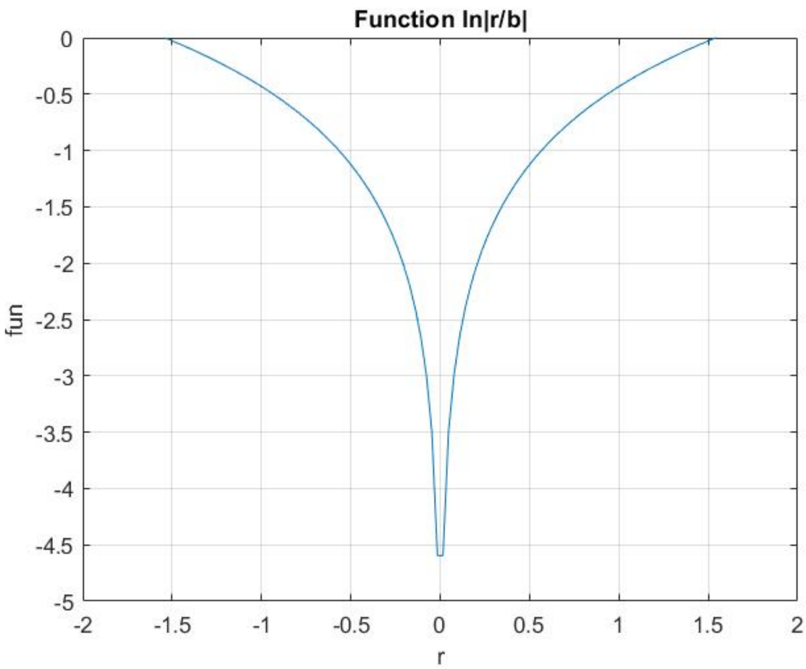

Figure 4.8: Plot of the function $ln|r/b|$, obtained with the parameters of the study case punch.

This explanation can also justify the different shape of the virgin curve for the considered geometries, linear when the integral part is negligible and polynomial when this one prevails.

4.4 Dimensional results

For the purpose of comparison with FEM data, a dimensional plot of the hysteresis loop evaluated with study case geometry has been provided in figure 4.9 for positive values of tangential load per unit length.

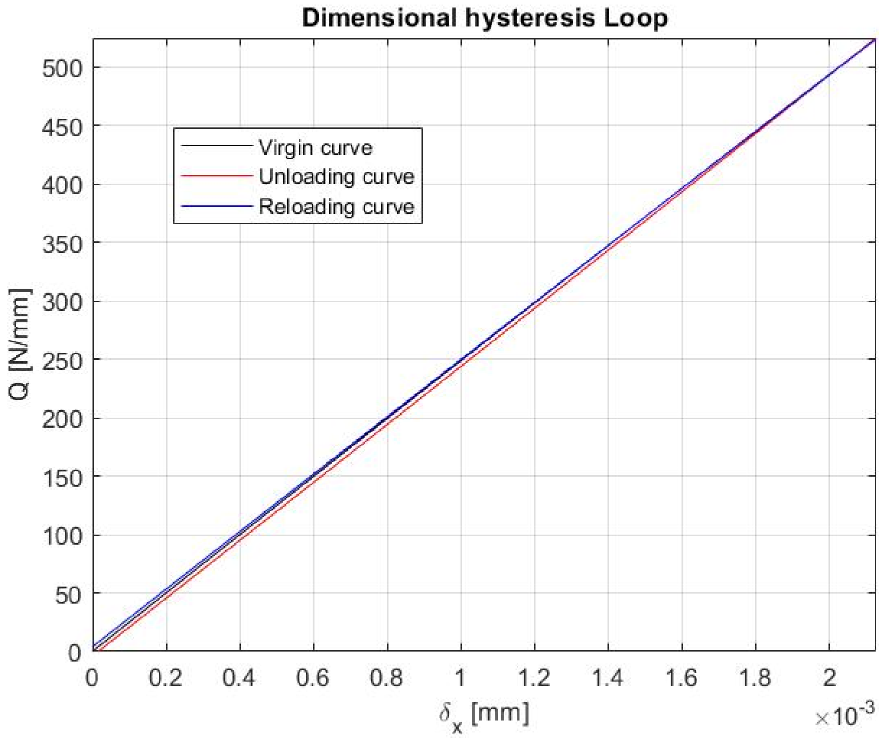

Figure 4.9: Hysteresis Loop for microslip regime using the problem's geometry with dimensional parameters.

Chapter 5

Contact Tangential Stiffness

5.1 Derivation from the virgin curve

As pointed out during the introduction, the contact stiffness k_t establishes a relationship between the applied load $T = Q \cdot L$ and the resulting displacement. A non linear relationship has been provided in equation 4.9, but now the purpose is to find k_t, using the following type of equation

$$T = k_t \cdot \delta \quad \rightarrow \quad k_t = \frac{dT}{d\delta} \tag{5.1}$$

The contact tangential stiffness can be obtained by simply deriving the virgin curve. However, it is not very straightforward to derive an implicit integral equation, so the finite difference method has been used. This method is described by the following equation

$$f'(x) \simeq \frac{f(x+h) - f(x)}{h} \tag{5.2}$$

For an equally spaced set, with spacing distance h. the results are displayed in figure 5.1.
As expected, being the virgin curve a straight line for different values of L, the contact tangential stiffness keeps practically constant throughout the monotonic tangential loading. Moreover, k_t drops as the ratio L/b increases, due to the decreasing slope of the virgin curve with increasing indenter length seen in previous chapter. However, a different behavior is found evaluating the contact stiffness for the usual rounded geometry, as shown in figure 5.2. For low values of indenter length, the contact stiffness is not constant and falls when Q tends to the maximum. But it is found also that for high values of L, the behavior of the k_t curve is essentially the same of the first case, i.e. the contact stiffness keeps almost constant. This might indicate that, when the indenter is much more wide than long ($L/b >> 1$), its shape does not affect anymore the relationship between the applied load and the relative displacement.
It seems then right to point out that the curves plotted in figures 5.1 and 5.2 follow the microslip regime hysteresis loop, so can not exist for values of $\delta > \delta^*$. However, if the gross slip regime is considered, the tangential load Q can not exceed the maximum value $Q_{max} = \mu \cdot P$, while the punch starts sliding with rigid body motion. In that case, $Q = Q_{max}$ is constant and δ increases, so that the contact stiffness falls, according to the equation 5.1.

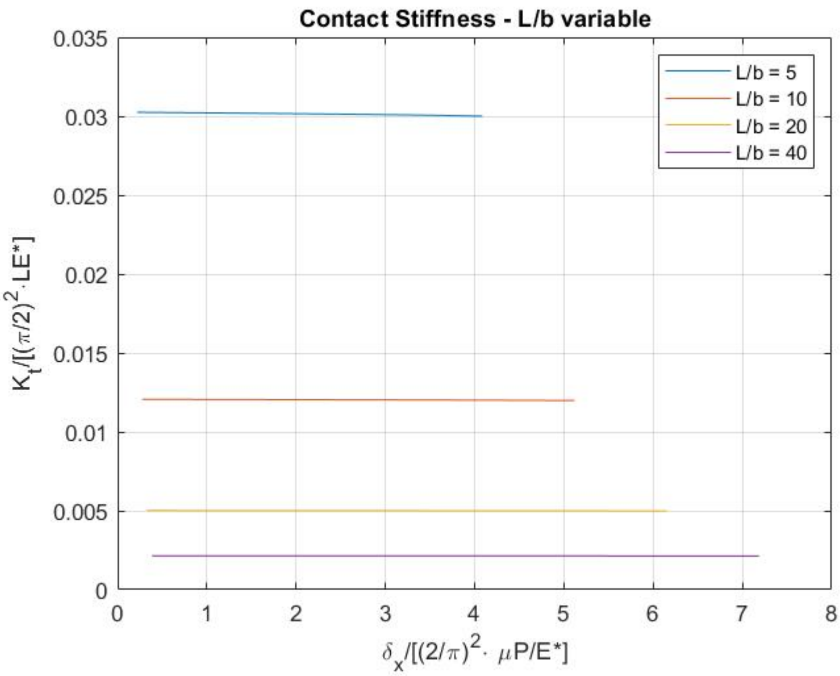

Figure 5.1: Contact tangential stiffness for variable values of indenter length.

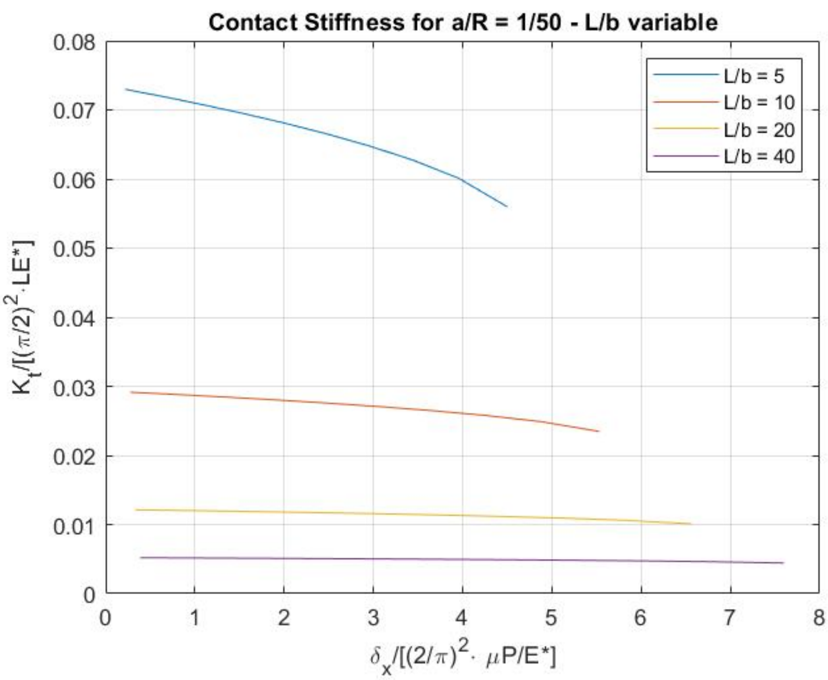

Figure 5.2: Contact tangential stiffness for rounded geometry and variable indenter length.

5.2 Dimensional results

As previously done, dimensional results for tangential contact stiffness are provided in figure 5.3. It could seem strange to see the tangential stiffness varying along the x axis, while non-dimensional results stated its constancy. This is due to the fact that only one curve is plotted, and the program focuses the axes in a restricted portion of the plane. So, undoubtedly k_t is not constant, but its variation is relatively insignificant if compared with other curves, evaluated for a rounded geometry.

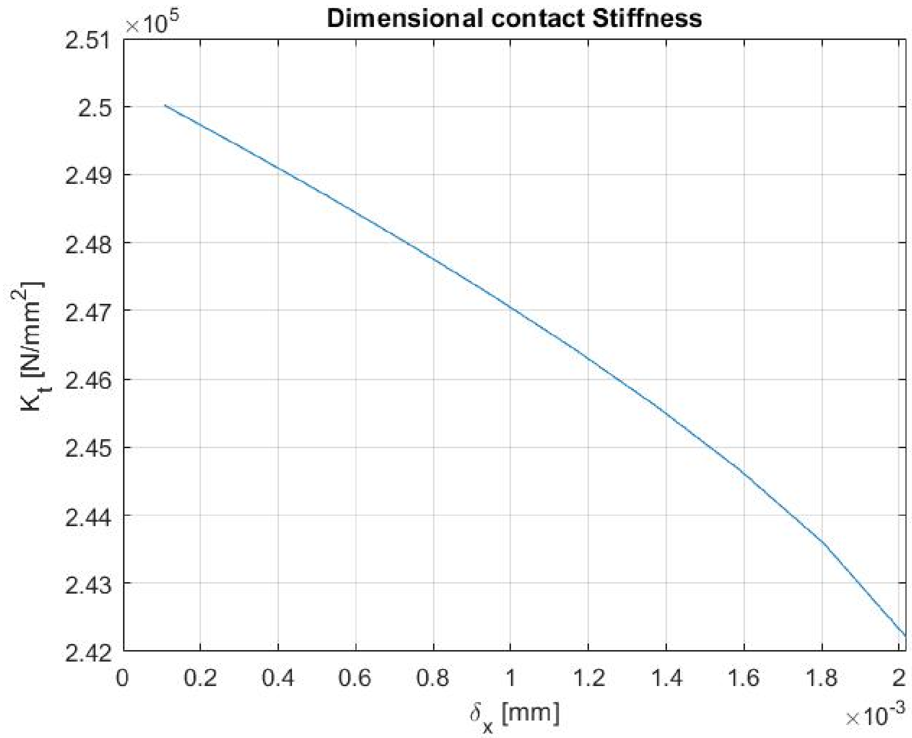

Figure 5.3: Dimensional contact tangential stiffness for study case geometry.

5.3 Tangential stiffness for variable normal load

Another important result to be shown is the relationship between the tangential stiffness and the applied normal load $N = P \cdot L$. The two graphs displayed in figures 5.4 and 5.5 put in evidence the influence of normal load for variable punch geometries and indenter length. Knowing that the higher is the ratio a/R the sharper is the edge of the punch, it is found that in all cases k_t grows with N and assumes lower values for rounded shapes. It means that an Hertzian geometry will be more deformable than a flat one. Moreover, it is found that the more the indenter is wide, the more easily it can be deformed, and the normal load does not affect k_t.

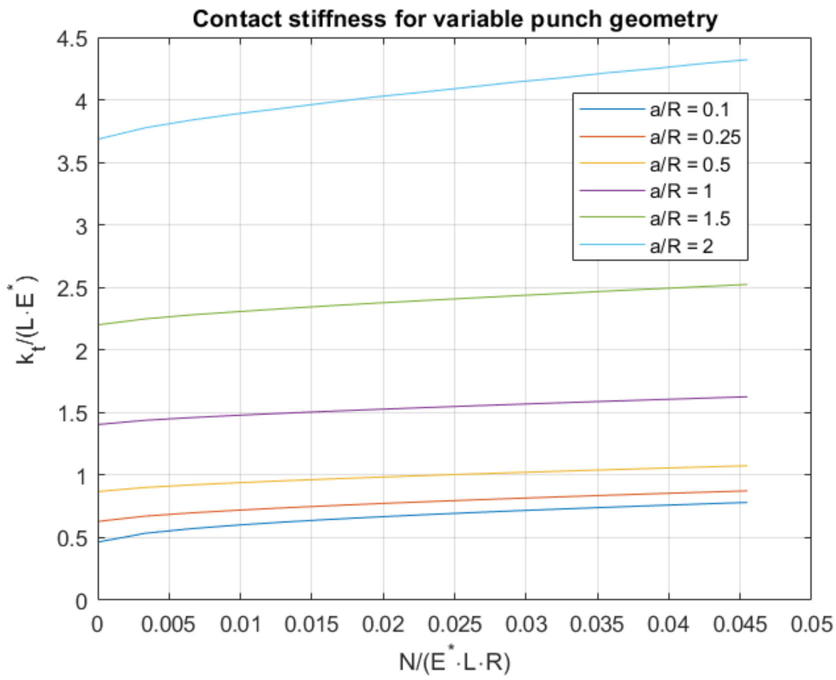

Figure 5.4: Contact tangential stiffness vs P for variable punch geometry.

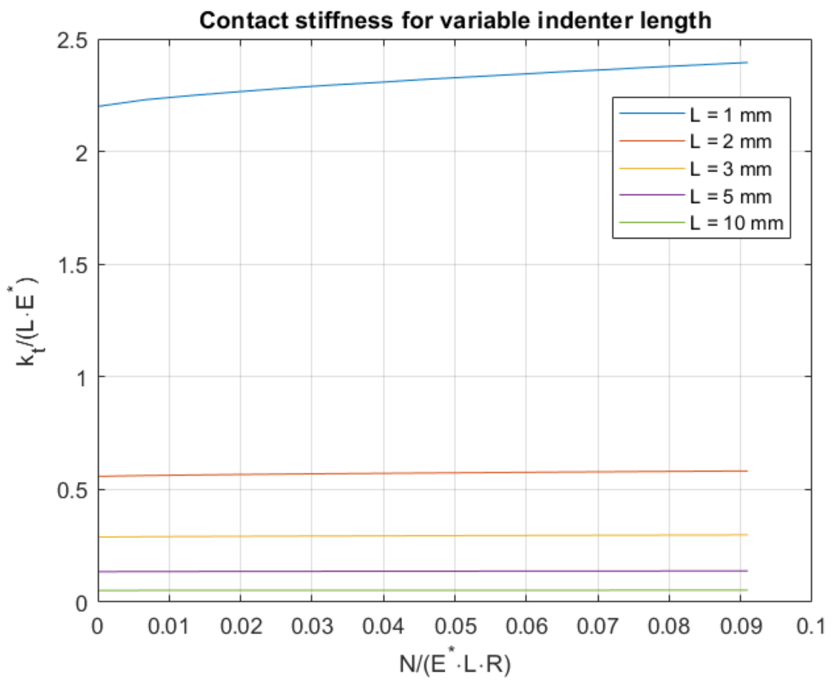

Figure 5.5: Contact tangential stiffness vs P for variable indenter length.

Chapter 6

FE model analysis and results

6.1 Introduction

After studying the analytical theories provided by literature and founding some interesting results in terms of stresses, displacements and contact stiffness, from now on the FE model of the defined system will be described and analyzed. In this part, a 2D model will be considered, formed by a rounded-end punch pressing against a rectangle (representing the infinite half-plane present in the analytical theory), which is much more wide than the overlying punch.

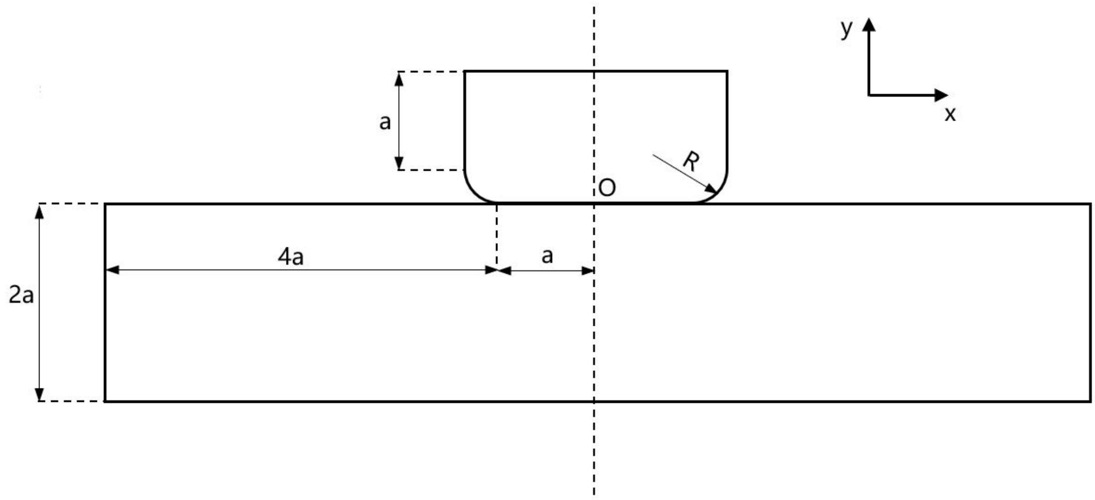

Figure 6.1: Geometry of the 2D FE model.

In figure 6.1, the complete geometry used for analysis is shown, with all of the dimensions necessary to fully describe it. The analytical theory does not prescribe a predefined size for all the geometric parameters, such as punch height, because these seem not to affect the final solution. So, coherent values were assigned to unknown sizes when the 2D CAD model was built. For instance, the flat body extends itself beyond the punch for a length of $4a$, in order to avoid the edge effects, that could influence the final solution.
Accordingly with theory, the origin of the reference system, which axes are displayed in figure 6.1, is the center of the contact stick zone, marked with the point O. Obviously, the geometric parameters a and R are the same of the analytical model.

Every FEM software requires three phases to acquire the requested data, process them and display the desired results:

- **Pre-processing**: Definition of the problem by Finite Element model;
- **Processing**: Solution of the system;
- **Post-processing**: Interpretation and representation of results;

These stages will be described later for each type of problem that will be analyzed, starting from the normal contact and then passing to the tangential one.

6.2 Normal Contact

6.2.1 Parameters setting

The preprocessing phase is a common base for the two load cases that will be studied, so it will be described once in present section. The system geometry, shown in figure 6.1 has been recreated with CAD software, integrated with the FE program. The two bodies, represented as areas in 2D, were defined by keypoints, lines and arcs. Two additional keypoints were put symmetrically in the rounded part of the punch, approximately in the zone where the contact ends. These points will be used in the post-processing phase. After defining the system geometry, the FE solver requires material data, element types, and meshing. All of the parameters set during the preprocessing stage are shown in table 6.1.

Table 6.1: Material constants and parameters set as input for the FE solver.

Element Type	PLANE183
Young Modulus	$2 \cdot 10^5\, MPa$
Poisson Ratio	0.3
Model Thickness	$1\, mm$

The particular element type chosen for the FE analysis is called *PLANE183*, a higher order 2D 8-node or 6-node element [9]. The reason is the fact that *PLANE183* has quadratic displacement behaviour and is well suited to modeling irregular meshes. This choice is extremely important when the meshing part will be discussed. Moreover, this element has only two degrees of freedom at each node, that are horizontal and vertical translation, u_x and u_y.
For what concerns the material, a common structural steel has been chosen, linear and isotropic, in order to keep the results as near as possible to the analytical solution.

6.2.2 Meshing

Mesh generation consists in creating a polygonal or polyhedral mesh, that approximates the geometric domain in study. As a 2D model is studied, the mesh will be polygonal, with possible degeneration in triangles. A polyhedral mesh is employed only for 3D geometric domains. At first, the element size must be set, i.e. the absolute dimension of the single element in the grid. For regions far from the contact zone, where knowing the solution is not requested, a size was chosen of 0.6 mm. It means that the mesh will be coarse and the solution will be then inaccurate, in order to save calculation resources, to be used where precision is requested. On the contrary, the grid has been refined in all the lines of the two bodies where the contact develops, like the flat part of the punch, its rounded edge and the upper part of the flat in proximity with the punch. In each of these regions, precision and accuracy is required, so the mesh will be fine and a lot of computing capacity of the calculator will be employed to solve the numerical matrices. The resulting mesh is shown in figure 6.3. It seems important to notice that, knowing the analytical solution, the flat part is not as fine as the rounded one. This is because in the central stick zone the shear traction and the normal pressure does not vary at all, while, at the beginning of rounded region, the pressure spikes represent a significant variation of the solution in a very small distance. This requires a finer mesh, in order to completely capture the pressure evolution and display it in postprocessing phase.

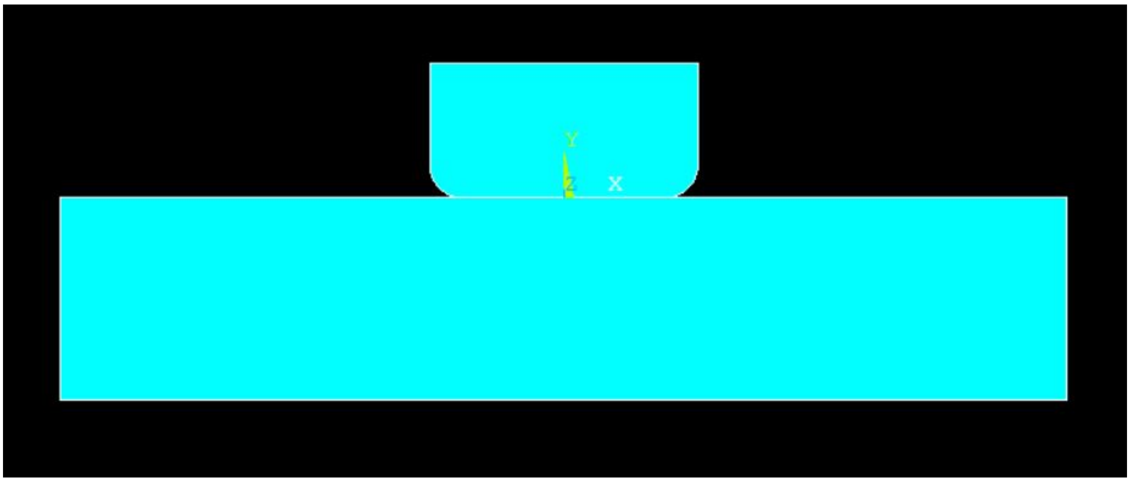

Figure 6.2: Geometry of the 2D FE model from FEM solver Grafic User Interface (GUI).

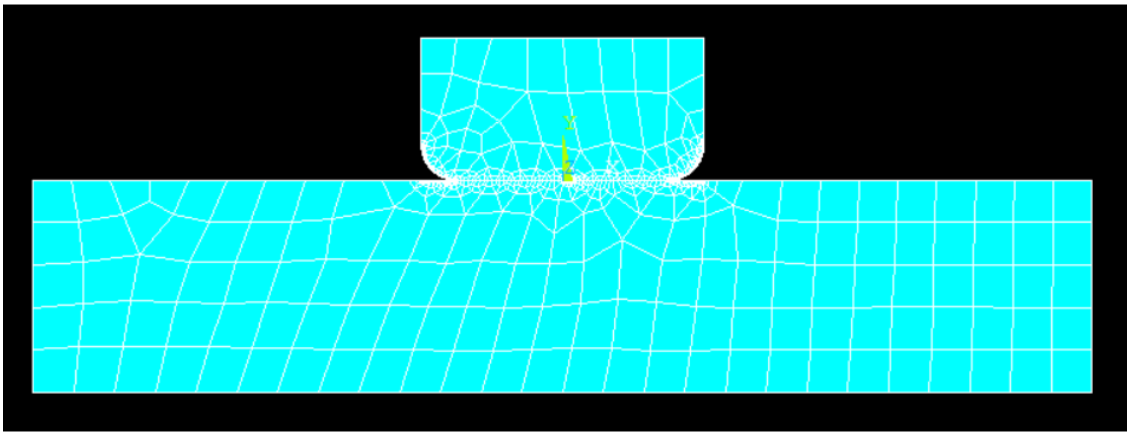

Figure 6.3: Meshed 2D model from FEM solver GUI.

6.2.3 Contact Pair creation

During a contact analysis, after the generation of geometry and mesh, it is necessary to identify the contact surfaces and define them via target and contact elements, which will then track the kinematics of the deformation process [9]. In order to achieve the best solution in terms of CPU time, the contact zone must be as small as possible, following the same logic used for grid generation. So, at first, it is necessary to define a *Target Surface* (Flat body), which shape is described by the target segment element *TARGE169*, and a *Contact Surface* (Punch), defined by the contact element *CONTA172*. These elements are shown in figure 6.4.

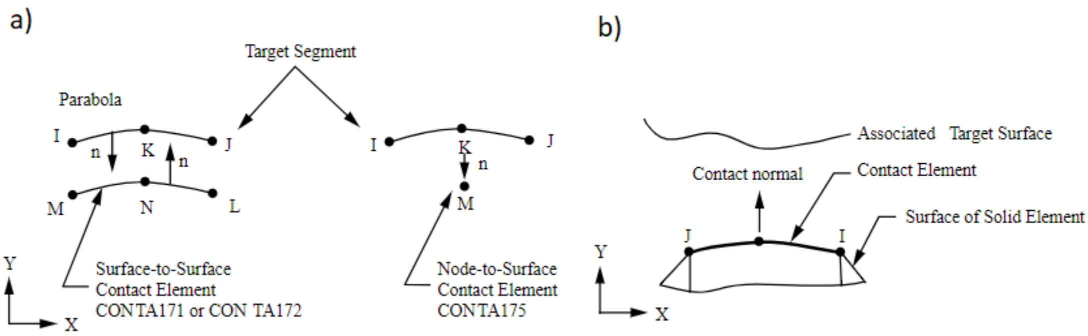

Figure 6.4: Schematics of *TARGE169* (a) and *CONTA172* (b) elements form Ref.[9].

For flexible targets, *TARGE169* overlay the pre-existent elements, describing the boundary of the deformable target body. Instead, *CONTA172* is used to represent contact and sliding between bi-dimensional target surfaces and a deformable surface and allows Coulomb friction assumption. It is important to notice that contact occurs only when the element surface penetrates an associated target surface. Finally, during the contact pair creation, the friction coefficient must be defined. In analytical theories, the tangential sliding due to a normal load is not considered, so, in order to obtain results as close as possible to the analytical ones, the friction coefficient must be zero and no shear traction is admitted.

6.2.4 Loads and constraints application

In this case, only a normal load per unit length is applied on the upper surface of the punch, which value is $P = 1050\,N/mm$. Knowing that the upper face has a width of $4\,mm$ and a depth of $1\,mm$, the line pressure is $p_0 = 262.5\,N/mm^2$. For what concerns the constraints, it is sufficient to prevent the horizontal displacement ($u_x = 0$) for the edges of the flat parallel to the y axis and the vertical one ($u_y = 0$) for the flat basement. What stated is displayed in figure 6.5.

6.2.5 Solution and post-processing

In order to solve the current system, a static analysis has been required from the FE solver. With all the necessary parameters set, the program can run and all the system matrices can be solved. For the post-processing phase, the path creation function has been used to display the desired results. After selecting some keypoints, lying in the contact zone, a new set of abscissa values has been defined by point interpolation. Then, thanks to a software tool, the normal contact pressure has been plotted, against the new set of points, and is shown in figure 6.6.
It seems that the problem has been well captured, because the shape of the curve is the same of the analytical one, with a quasi-constant pressure central zone and the two symmetrical spikes. In following chapter, a full comparison will be performed between analytical and numerical data. Finally, the structure deformed shape following the normal loading has been retrieved and is now displayed in figure 6.8.
It is easy to observe the entity of normal penetration, with respect to the original geometry, marked with dashed line. But it is more important to evidence the bowing of the upper line, where the normal load has been applied. This fact, not foreseen from the analytical theory, is

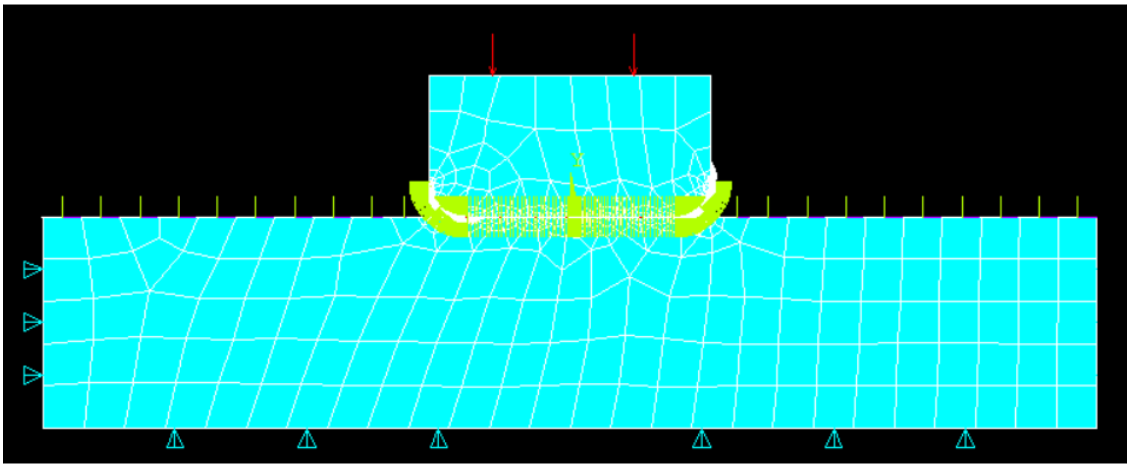

Figure 6.5: Meshed 2D model with loads and constrains applied.

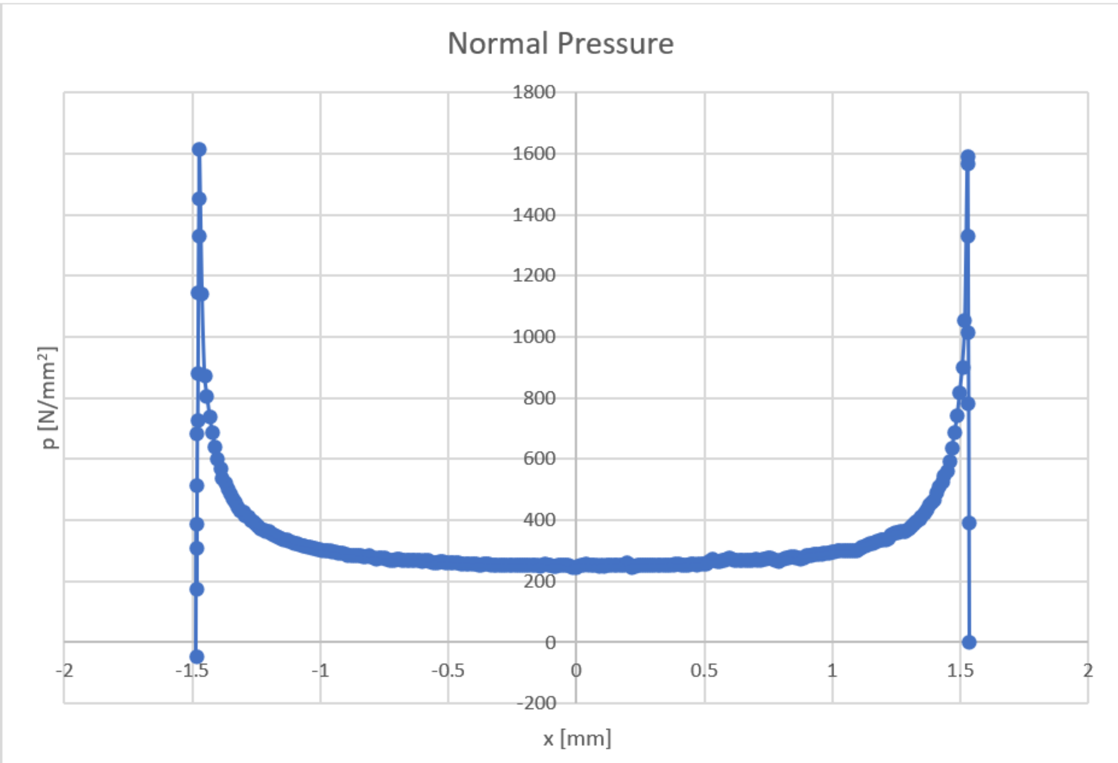

Figure 6.6: Numerical normal contact pressure.

due to the crushing generated by the normal load itself. Because of the absence of friction, this is irrelevant for normal contact case, as can be noticed in figure 6.7, but it will affect the shear traction in following sections.

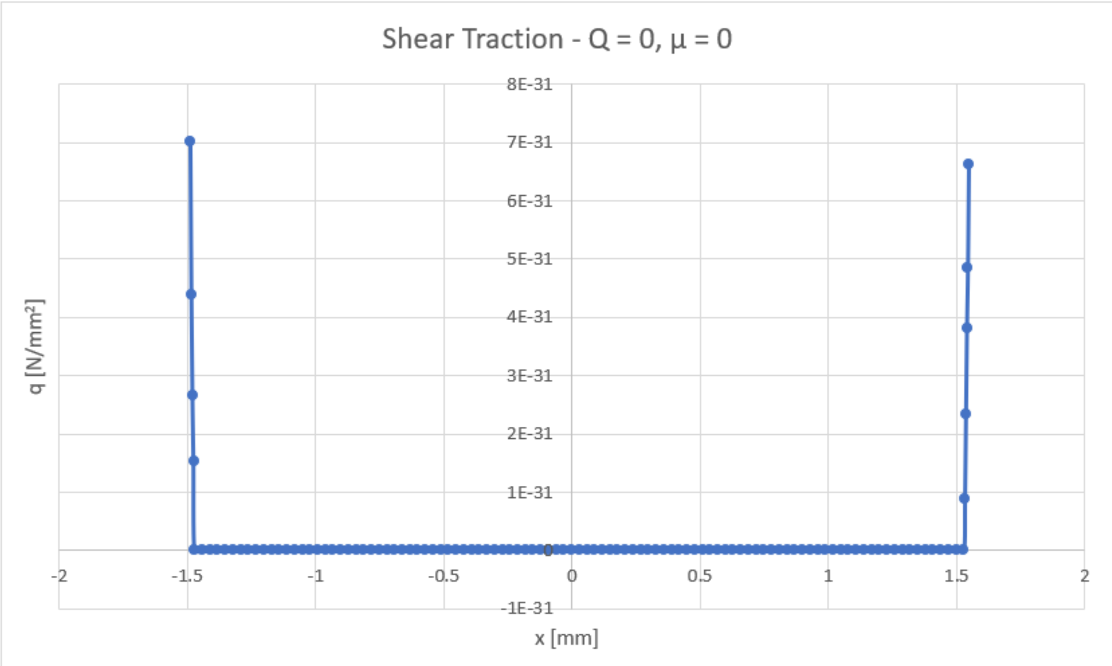

Figure 6.7: Shear traction for only normal load and $\mu = 0$.

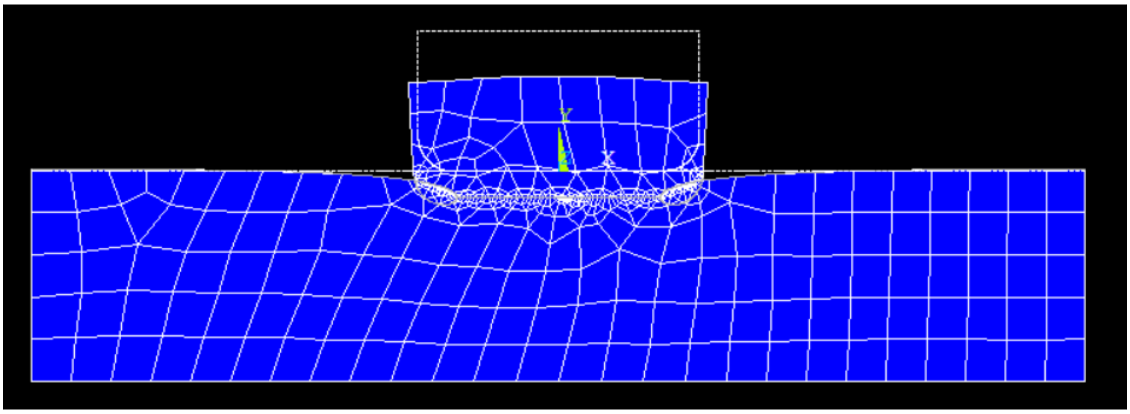

Figure 6.8: Deformed shape vs undeformed.

6.3 Tangential contact

6.3.1 First approach

Attention is now turned to the case of monotonic tangential loading with constant normal load and the goal is to obtain the shear traction curves, that allow to recreate the virgin curve and finally calculate the contact tangential stiffness. The pre-processing phase is almost the same of the previous case, because geometry and mesh remain unchanged. The only parameter that modifies is the friction coefficient, which value is now $\mu = 0.5$, as it was in analytical part. Moreover, while the structural constraints does not change, the tangential load must be added to the load system. However, the FE software employed does not support a directly applied tangential load per unit length, so a nodal load has been assigned to all the nodes lying in the upper surface (a line in 2D) of the punch. So, knowing the load Q to be applied, it has been distributed in equal parts to all of the described nodes. What stated is showed in figure 6.9, from the FE software GUI.

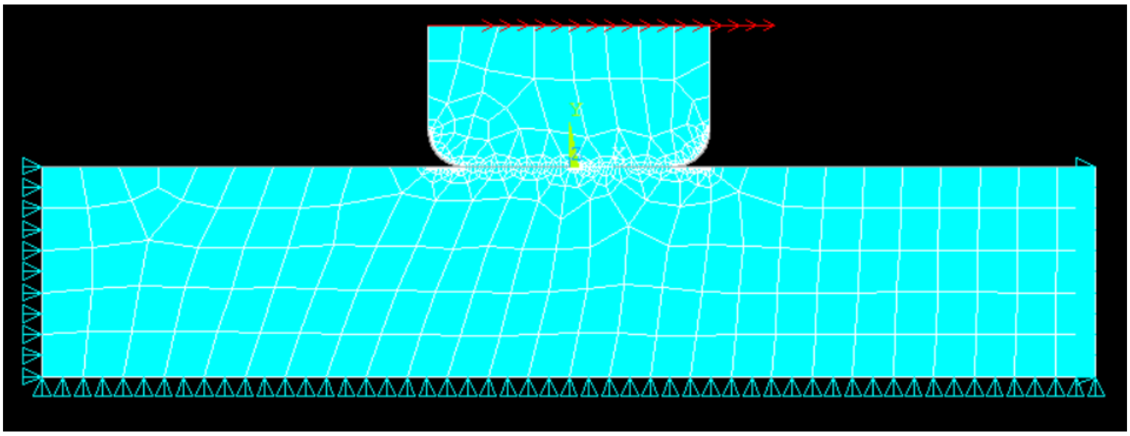

Figure 6.9: Meshed 2D model with tangential load and constraints applied.

The analysis results, obtained with the same post-processing settings of the former section, have been provided for increasing values of Q, from the unloaded case to the maximum value Q_{max}.

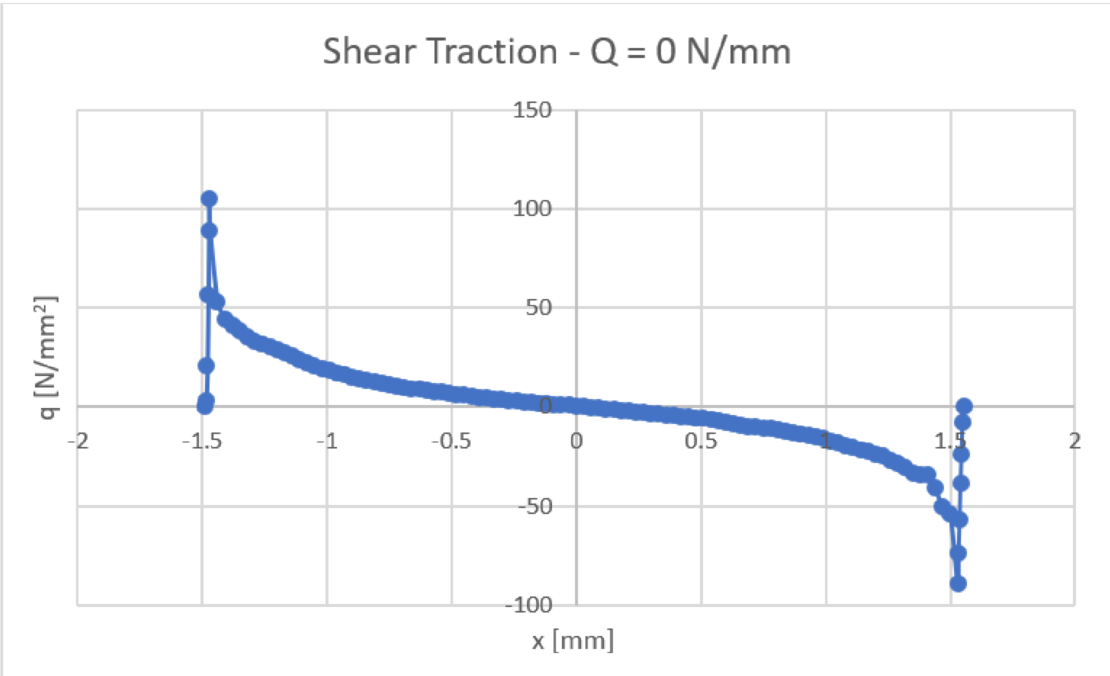

Figure 6.10: Resulting shear traction for $Q = 0\ N/mm$.

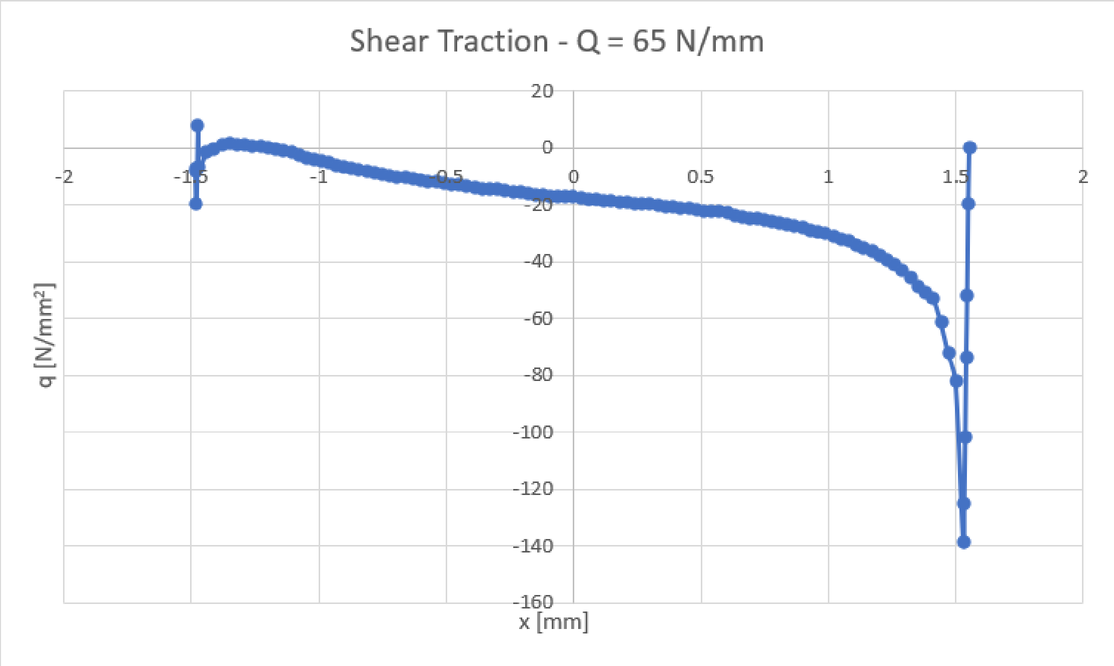

Figure 6.11: Resulting shear traction for $Q = 65\ N/mm$.

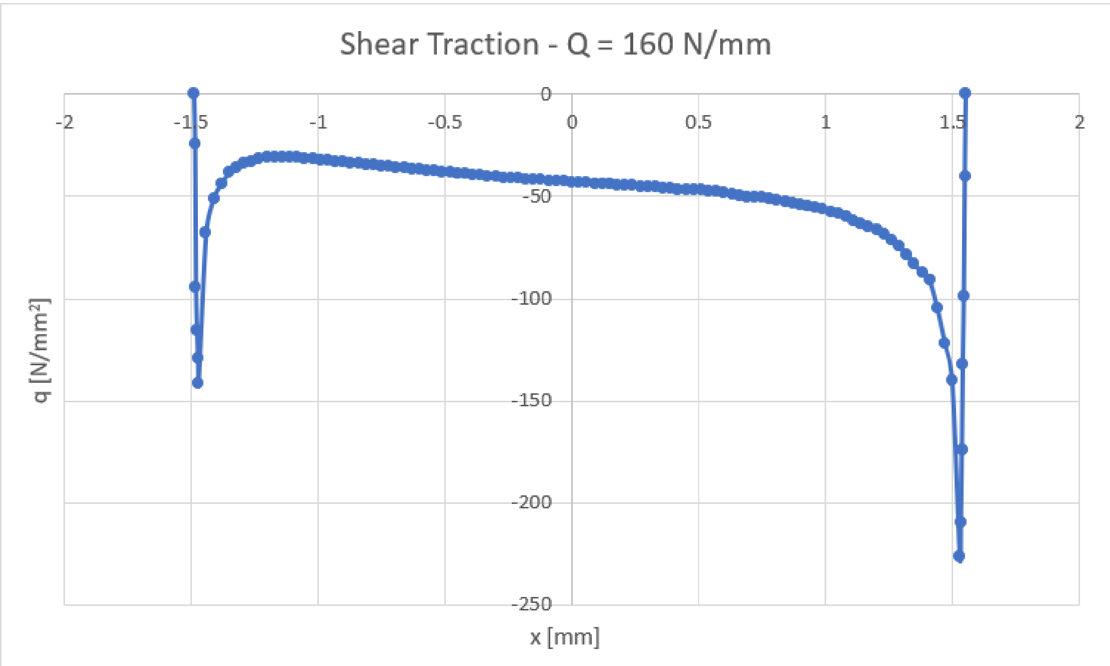

Figure 6.12: Resulting shear traction for $Q = 160\ N/mm$.

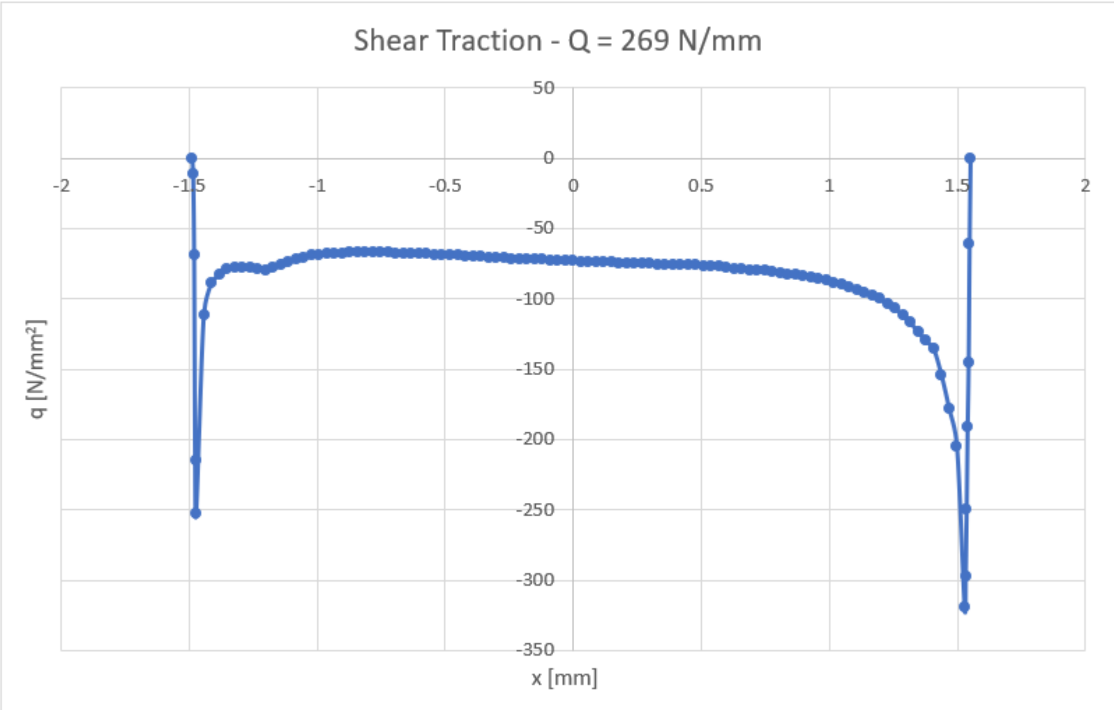

Figure 6.13: Resulting shear traction for $Q = 269\ N/mm$.

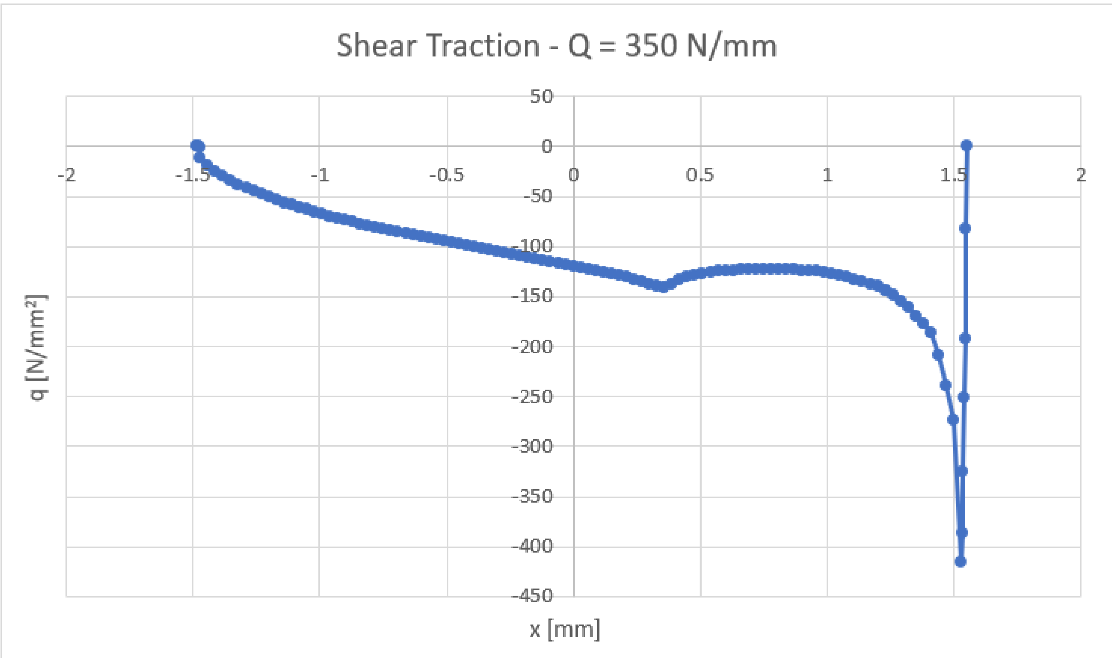

Figure 6.14: Resulting shear traction for $Q = 350\ N/mm$.

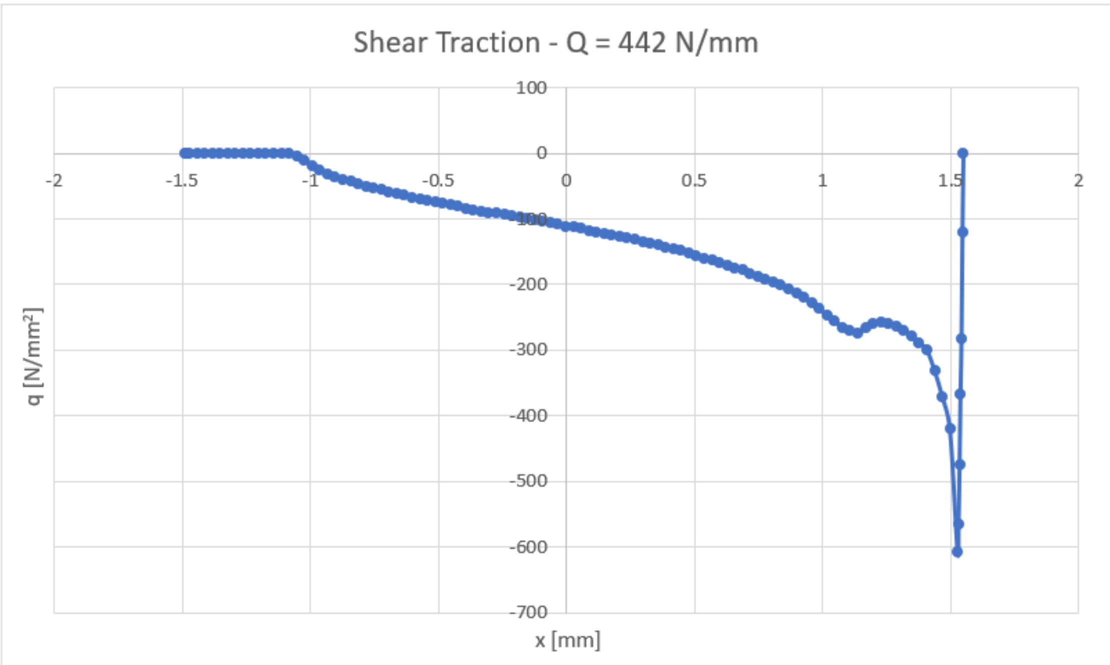

Figure 6.15: Resulting shear traction for $Q = 442\ N/mm$.

The obtained results clearly do not match with the analytical ones and the solution lose its symmetry, for the following reasons:

- The analytical theory does not admit the effects of the twisting moment caused by the tangential load Q. It is in fact responsible for partial detachment of the bottom left corner of the punch, for low values of Q, and total detachment of this part. It can be easily understood by figures 6.14 and 6.15, where q falls to zero in the left side of contact area. What stated is also proved by displacement state provided in figure 6.16.

- For $\mu \neq 0$, it can be noted from figure 6.10 that a quasi-symmetrical shear traction distribution exists even if no tangential load has been applied. This is due to P, responsible for the punch crushing, that generates an anti-symmetrical tangential pressure, according to the scheme in figure 6.17.

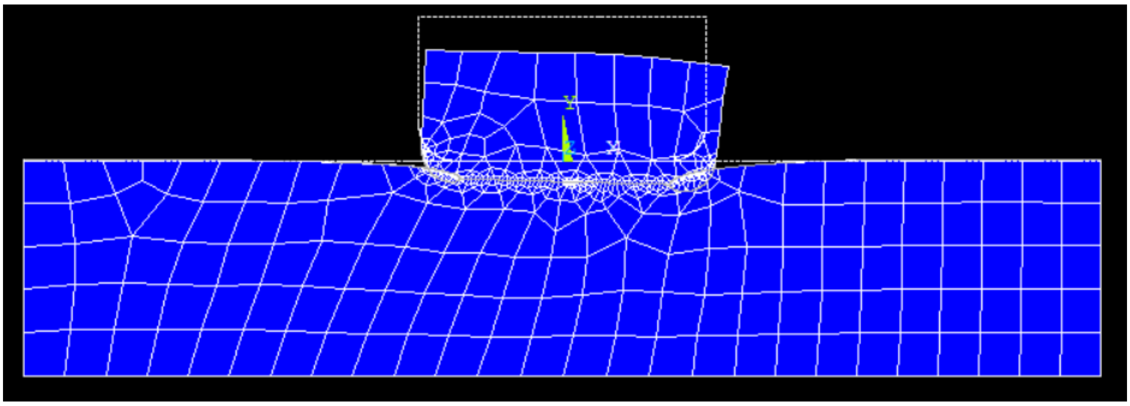

Figure 6.16: Deformed shape vs undeformed for both normal and tangential loading.

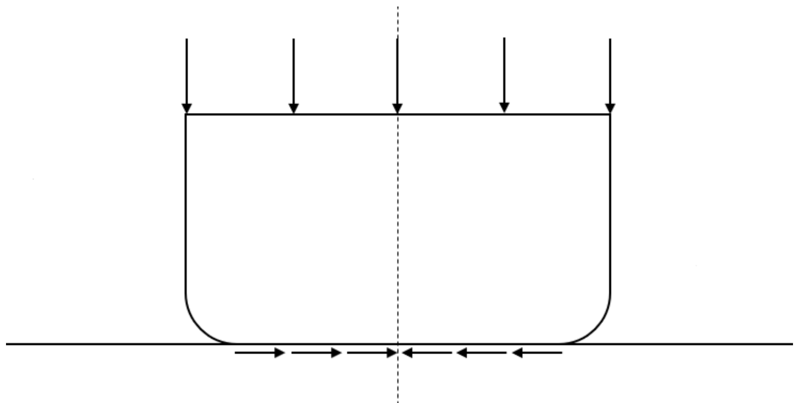

Figure 6.17: Schematics of shear traction generated by crushing.

All these facts together cause the punch to reach the gross slip regime for $Q \simeq 442\,N/mm$, instead of Q_{max}. Some corrective actions must then be taken, in order to make the FEM model comparable with the analytical one.

6.3.2 Second approach

It is necessary to compensate the effect of the twisting moment due to Q and the crushing effect due to P. It has been decided to block the vertical displacement u_y for all the nodes lying in the upper surface of the punch after the application of P. In this way, only the horizontal sliding will be possible for these points and the effect of line bowing will be significantly reduced. Moreover, thanks to the *RESTART* command, it is possible to calculate the normal solution with $\mu = 0$ and the tangential one resetting the friction coefficient to 0.5. The obtained results have been provided in the graphs displayed in following pages.
This time, there is no sign of premature detachment of the punch and the last value of tangential load recorded before the gross slip is $Q = 510\,N/mm$, that is very close to the theoretical $Q_{max} = 525\ N/mm$. Moreover, the shear traction for $Q = 0\ N/mm$ is almost zero, with low spikes at the edges of the contact, as shown in figure 6.18.
However, especially for low values of Q, q does not have a regular and smooth shape. This fact can be due to the already cited perturbations, which effect is not easy to fully wipe. But for increasing values of Q, these effects becomes more ad more negligible and q assumes a quasi-symmetrical shape, as can be seen in figures 6.23 and 6.24.

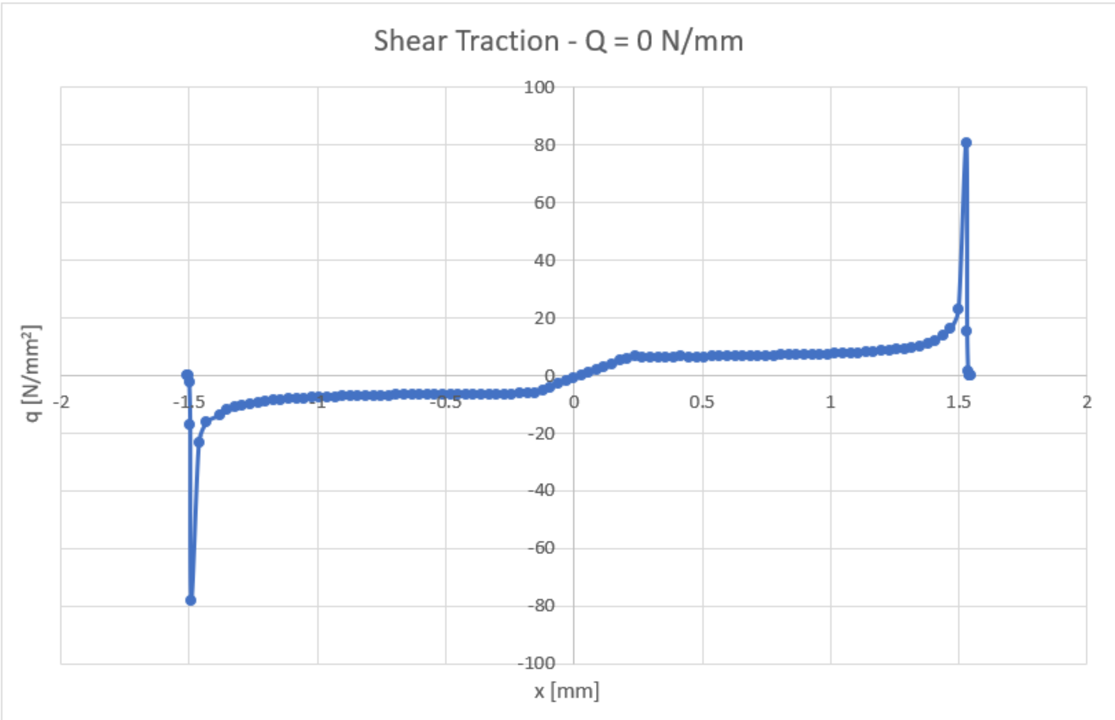

Figure 6.18: New resulting shear traction for $Q = 0\ N/mm$.

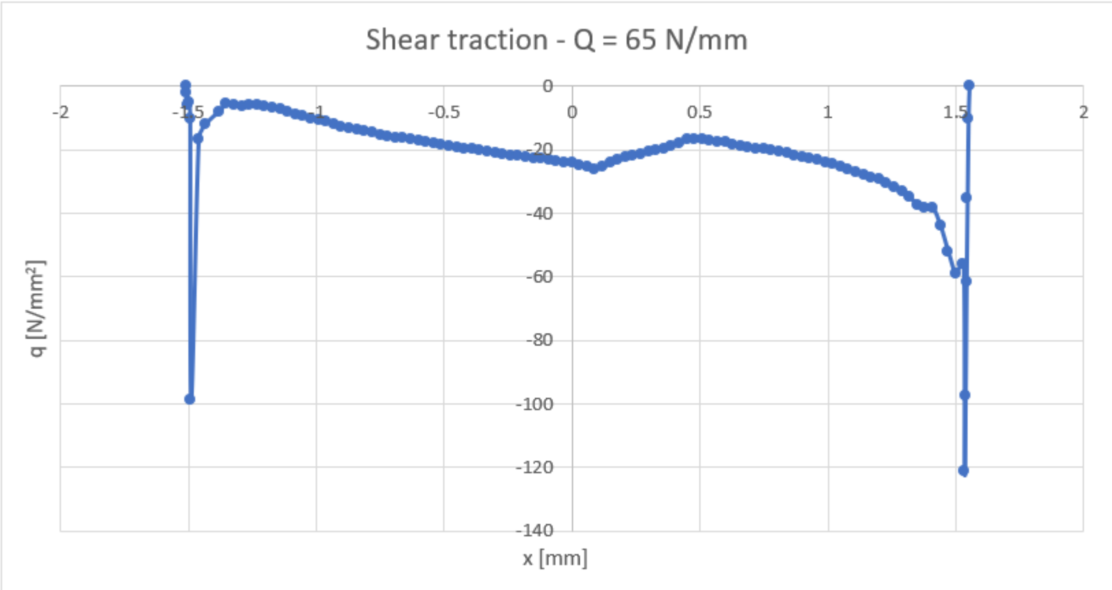

Figure 6.19: New resulting shear traction for $Q = 65\ N/mm$.

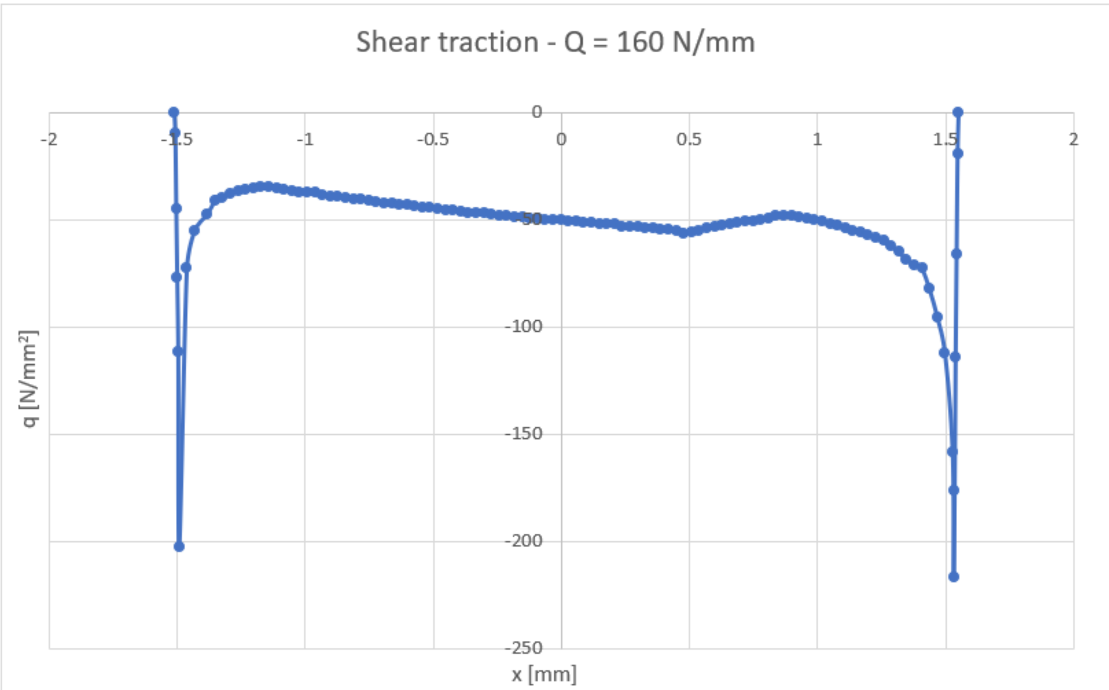

Figure 6.20: New resulting shear traction for $Q = 160\ N/mm$.

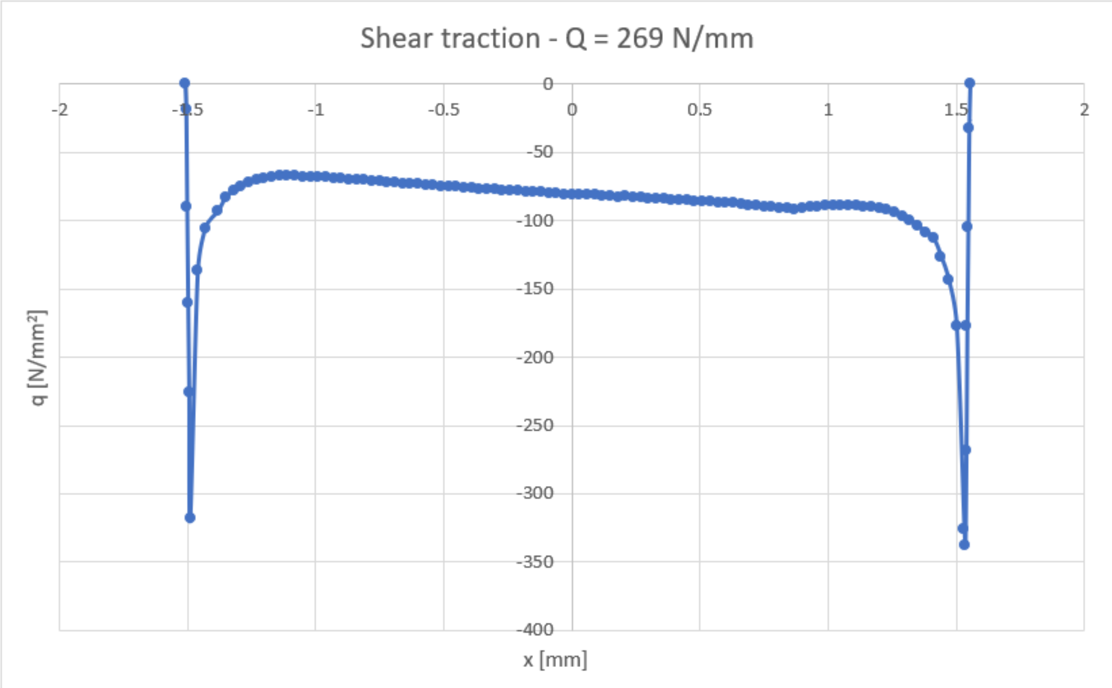

Figure 6.21: New resulting shear traction for $Q = 269\ N/mm$.

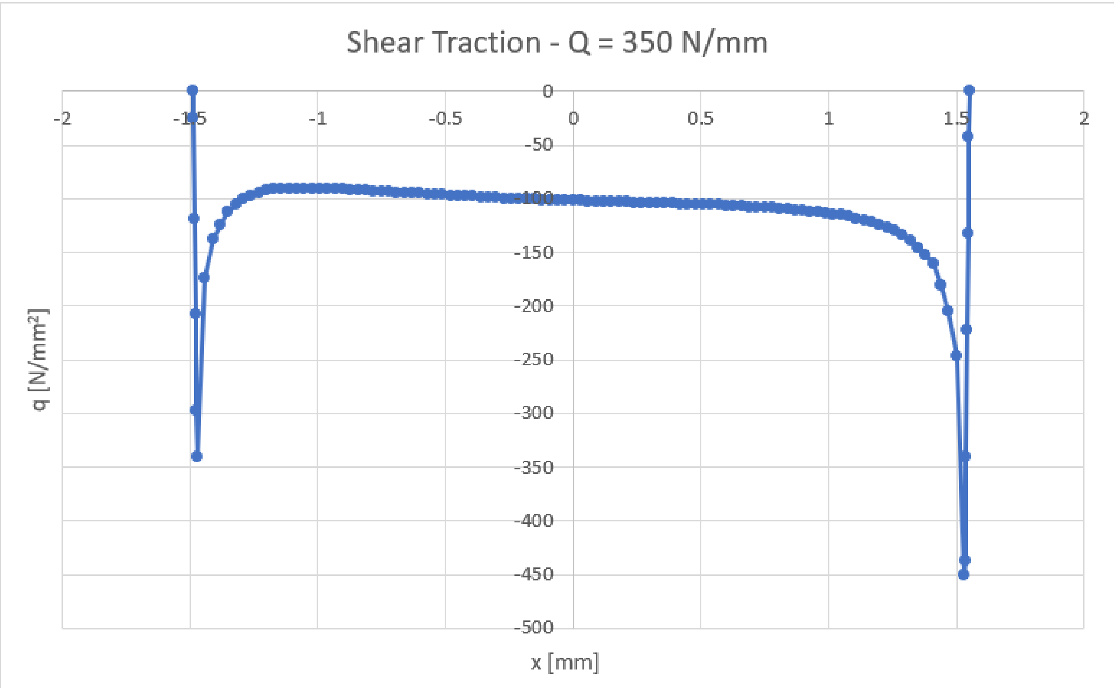

Figure 6.22: New resulting shear traction for $Q = 350\ N/mm$.

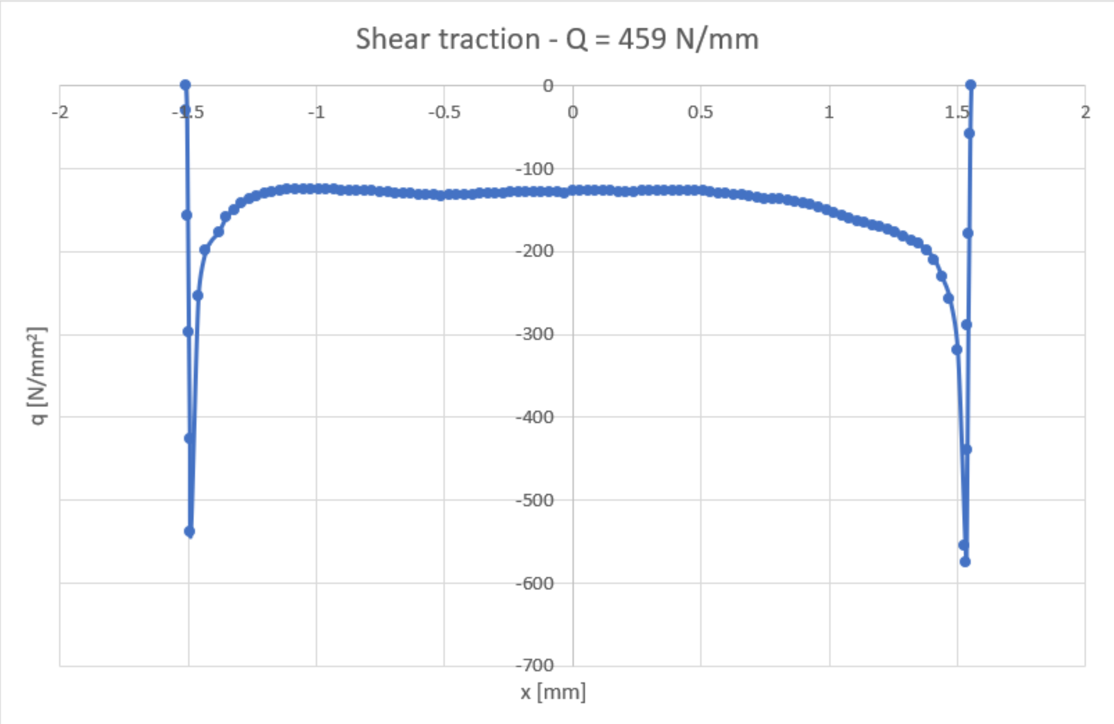

Figure 6.23: New resulting shear traction for $Q = 459\ N/mm$.

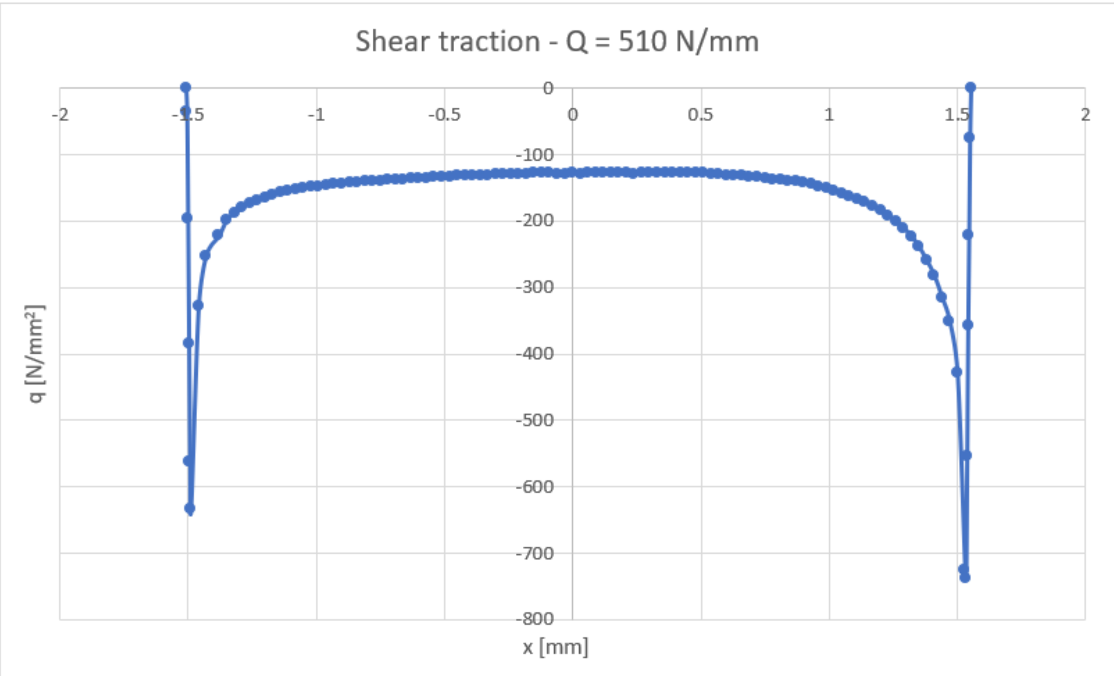

Figure 6.24: New resulting shear traction for $Q = 510\ N/mm$.

6.4 Virgin curve and tangential stiffness

The calculation of the virgin curve has been performed using the equation 4.9 and the numerically determined integrals of the curves obtained in previous section. It is right to point out that, according to the equation 4.8, the integral of the shear traction over the contact length must match the tangential load Q. Obviously, due to errors derived by numerical integration and FE analysis, the equation 4.8 is not satisfied, but the results found do not differ beyond 2-3% with respect to the analytical ones.

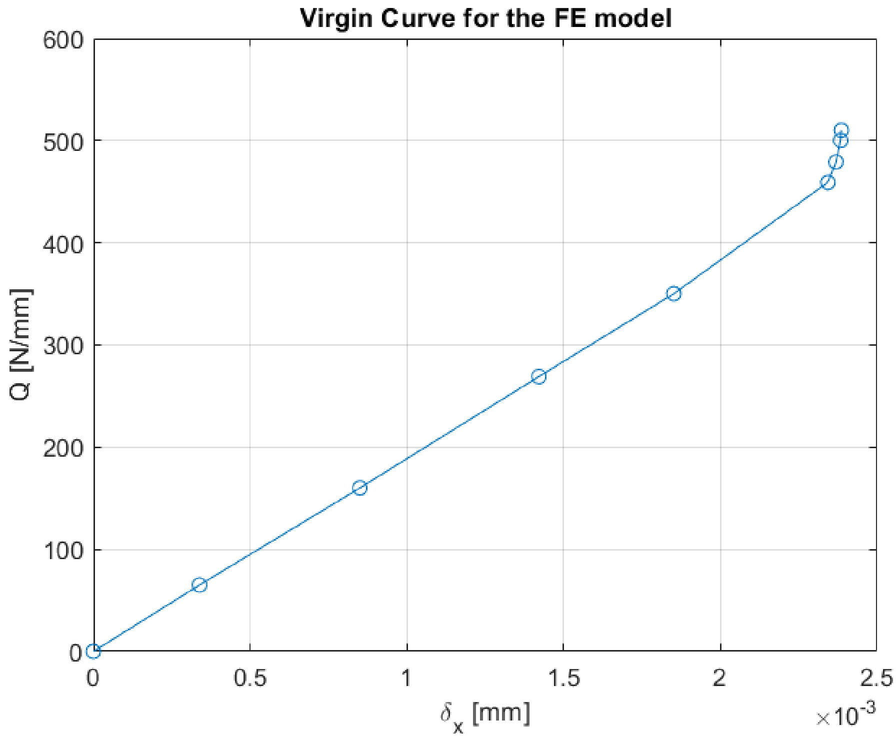

Figure 6.25: Virgin curve determined with FEM analysis.

The results are shown in figure 6.25 and 6.26. Evident differences with the analytical results can be spot at first sight, especially in proximity of Q_{max}, where the tangential stiffness tends to infinity. Moreover, the tangential stiffness has been evaluated in figure 6.27 for increasing values of normal load N, by taking the first value of slope of the virgin curve, calculated at every step of N. A more detailed comparison with the analytical results will be performed in next chapter.

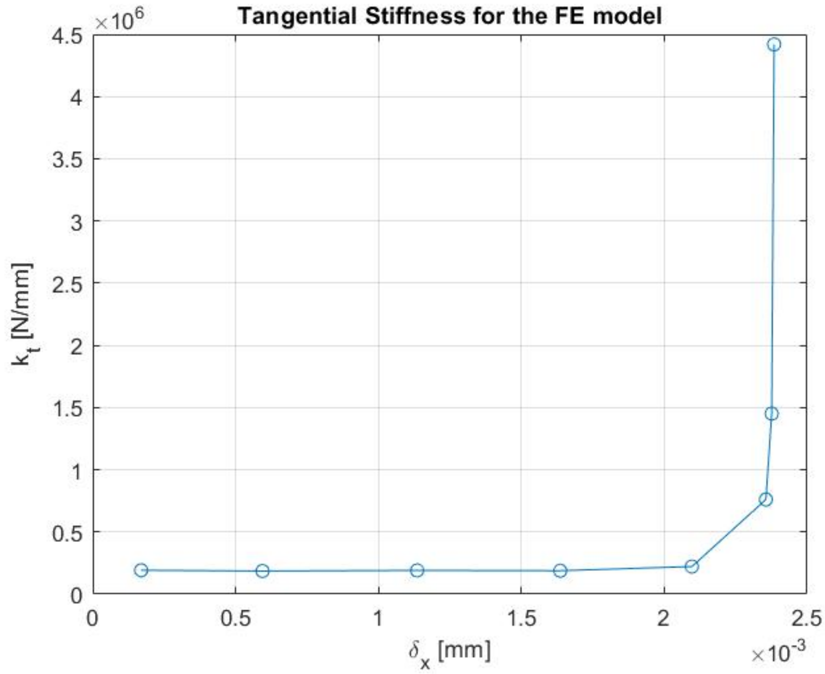

Figure 6.26: Tangential stiffness determined with FEM analysis.

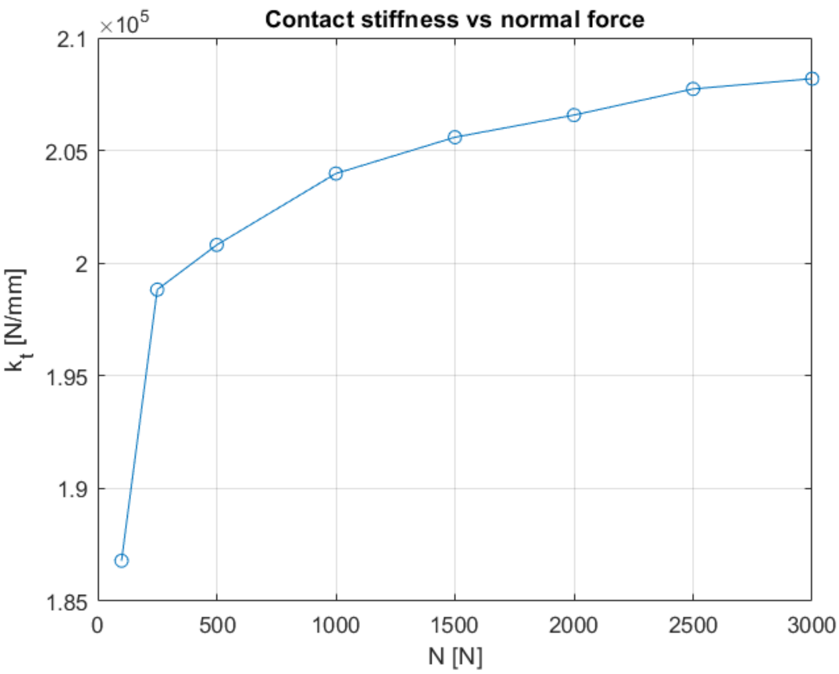

Figure 6.27: Tangential stiffness vs normal load.

Chapter 7

Comparison between numerical and analytical results

7.1 Normal pressure comparison

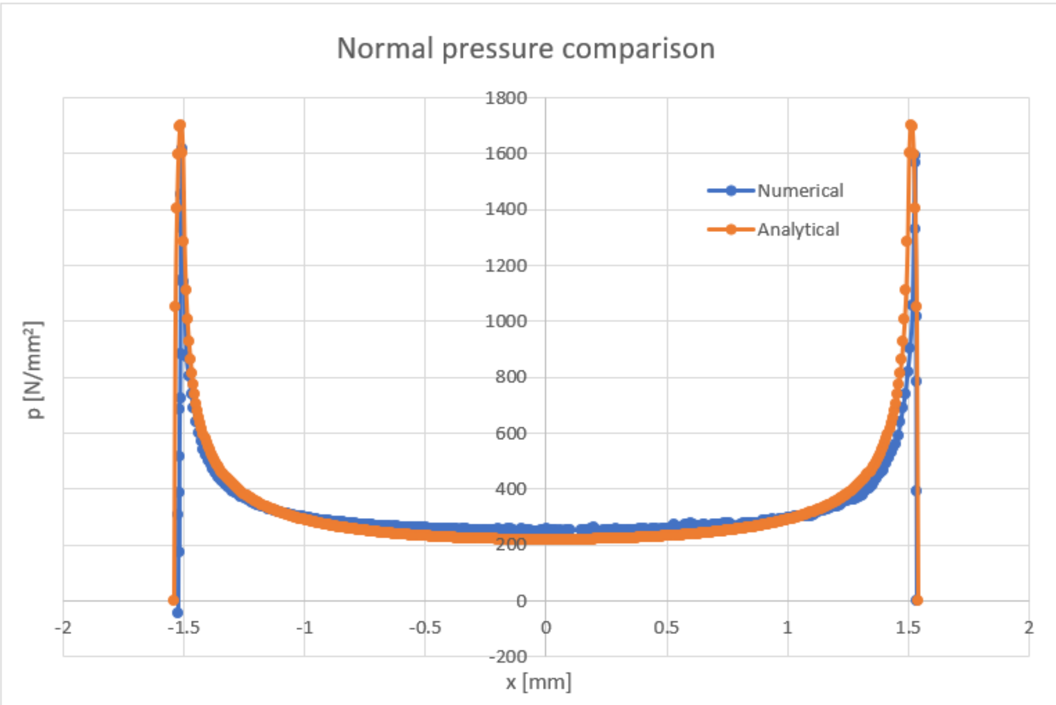

Figure 7.1: Comparison between numerical and analytical data for normal pressure.

The first data comparison, regarding only normal contact, shows the good matching between FEM and analytical theory, as can be seen from figure 7.1. The slightly lower value of the pressure spikes for the FEM solution is not relevant, because the limited computing capacity and the student edition software employed by the author can not assure an high precision level.

7.2 Shear traction comparison

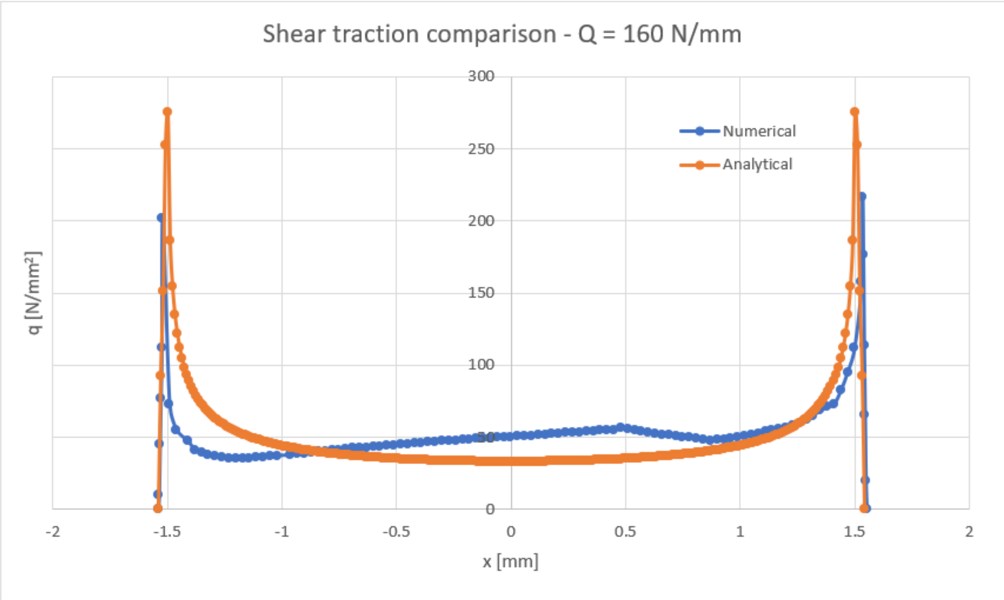

Figure 7.2: Shear traction comparison for $Q = 160\ N/mm$.

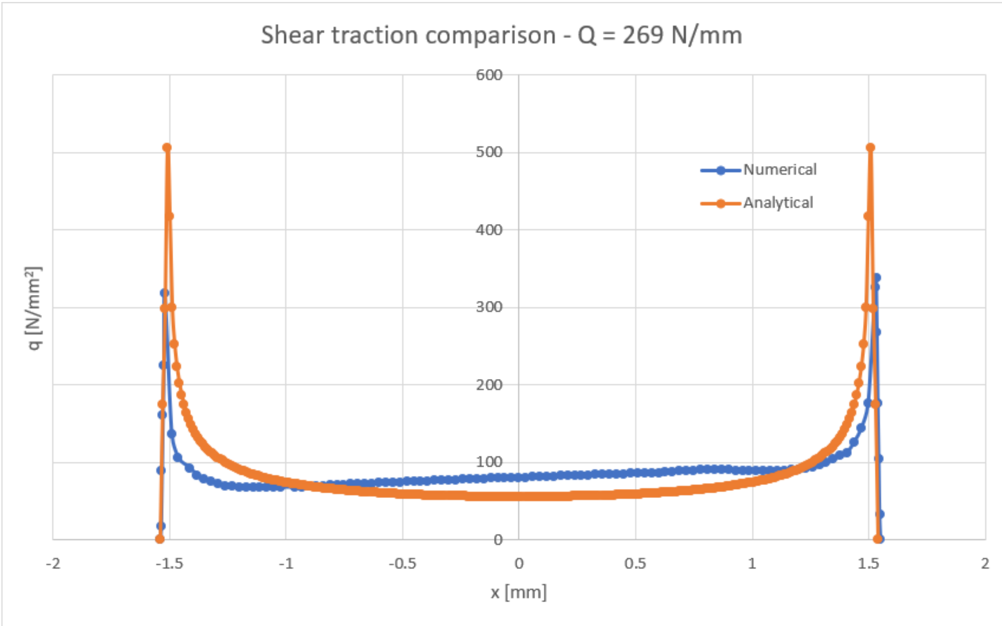

Figure 7.3: Shear traction comparison for $Q = 269\ N/mm$.

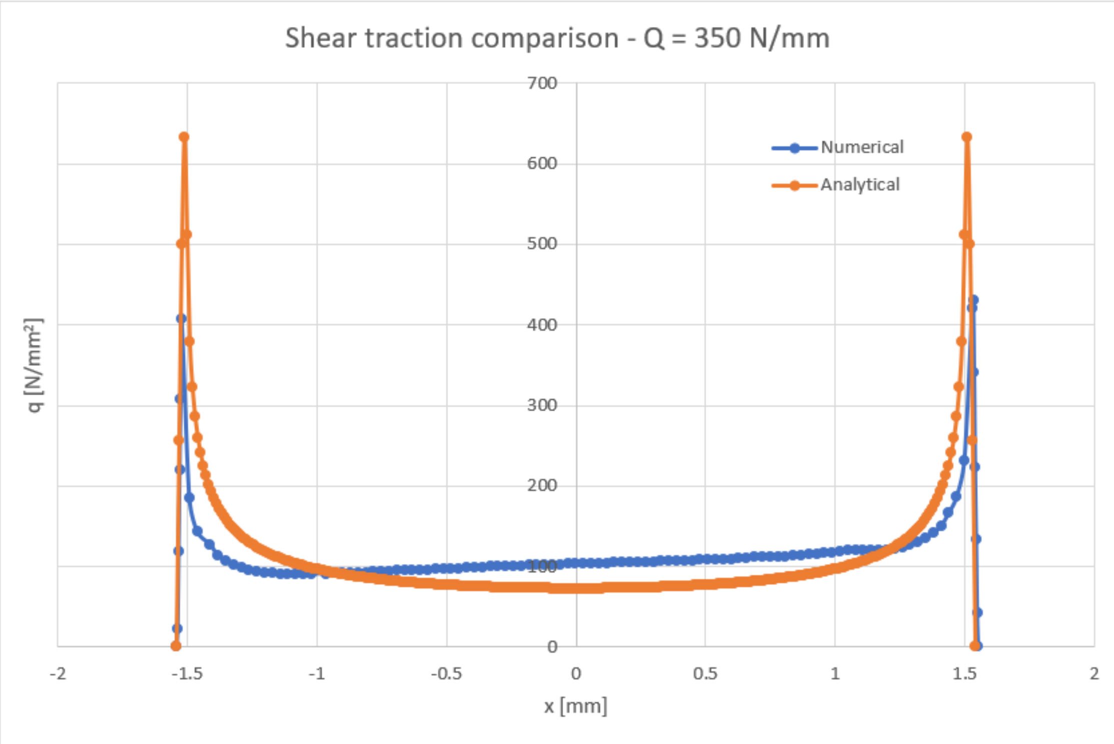

Figure 7.4: Shear traction comparison for $Q = 350\ N/mm$.

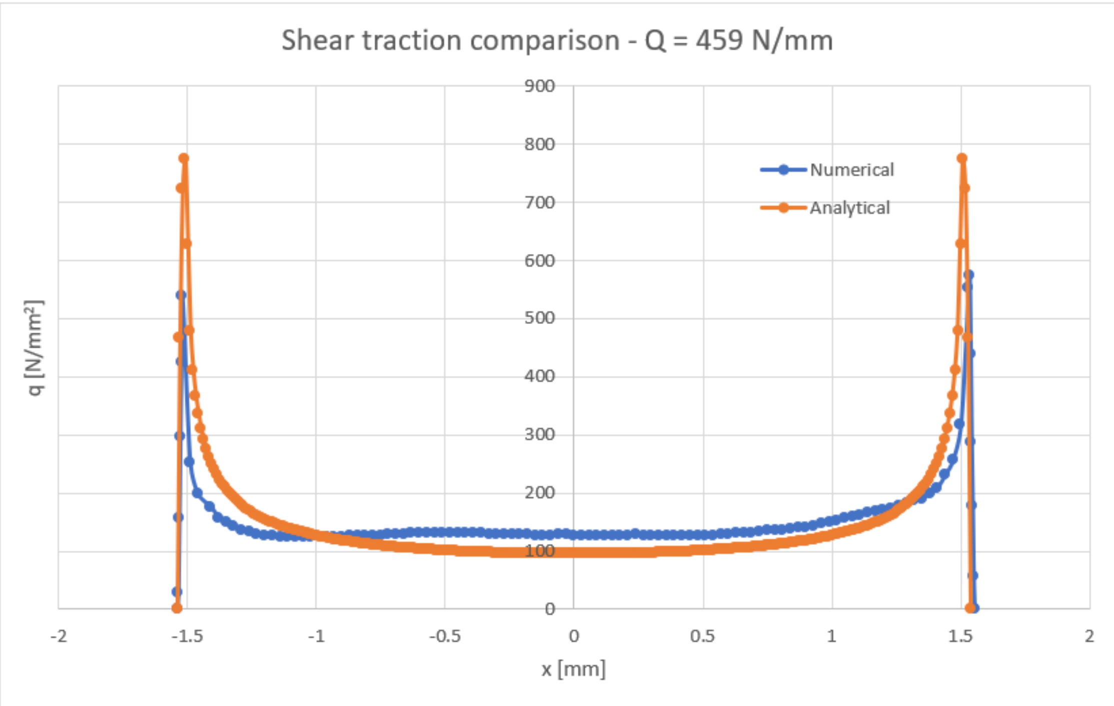

Figure 7.5: Shear traction comparison for $Q = 459\ N/mm$.

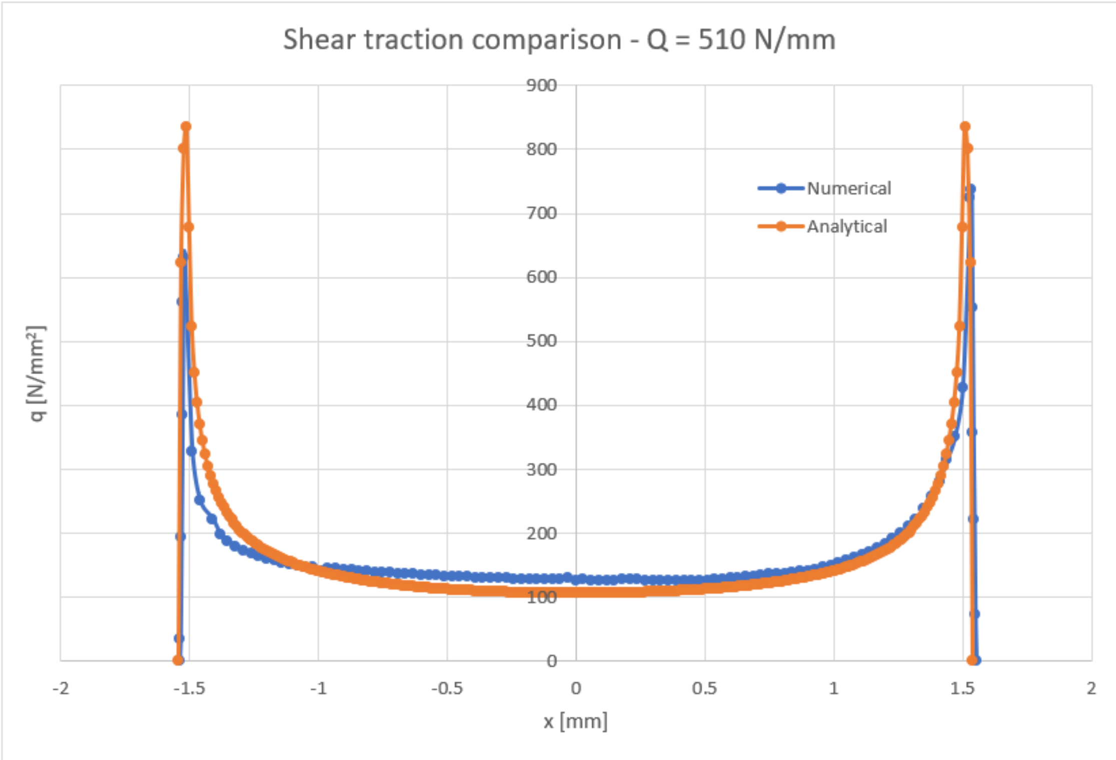

Figure 7.6: Shear traction comparison for $Q = 510\ N/mm$.

Although an almost symmetrical result is achieved for the shear traction curves, the edge spikes do not match the values of the analytical ones. This can be explained by the fact that a near limit case of theory is examined, sensitive to errors due to the preliminary assumptions. However, the central contact zone proves compliance between theory and FEM, especially for the last values of Q.

7.3 Virgin curve and tangential stiffness comparison

For what concerns the virgin curve, as can be seen from figure 7.7, in both cases the result is a straight line, but with different slopes. Indeed, theory provides a steeper curve, that means a less deformable behavior than in numerical case. This relationship is valid only until the last values of tangential load, where the FE curve assumes a vertical growth. In these points, there is a huge increase in contact stiffness and a very slow variation in relative displacement.
What stated is confirmed from contact tangential stiffness comparison shown in figure 7.8. Being the numerical virgin curve not perfectly straight, the tangential stiffness does not have a smooth trend, but its values are close enough to the ones provided by theory, except for the points close to the gross slip regime.
The last proposed comparison concerns the variation of the contact stiffness with normal load N, shown in figure 7.9. It can not be expected a full data matching, according to the previous comparisons, but the general trend of k_t is respected, except for very low normal loads.

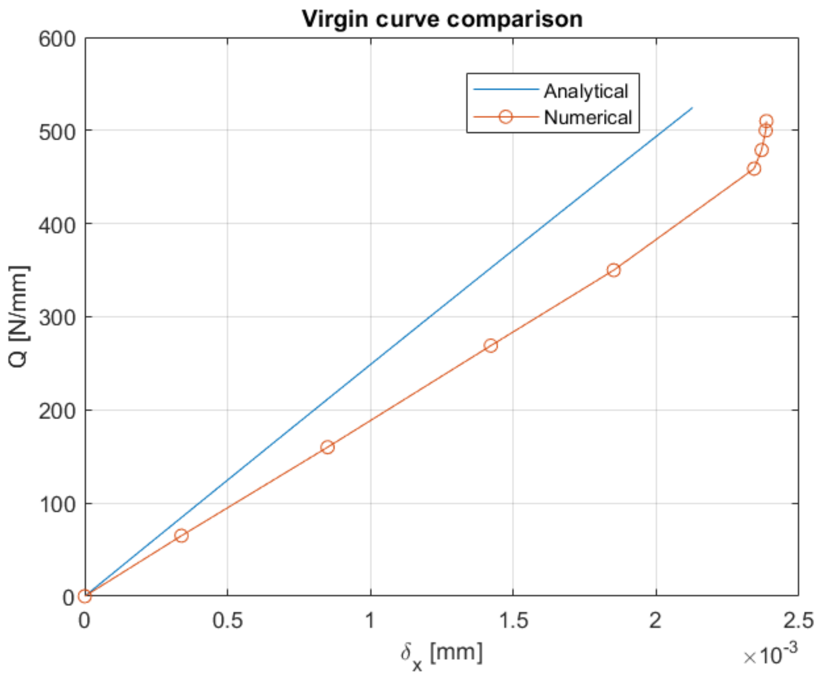

Figure 7.7: Virgin curve comparison.

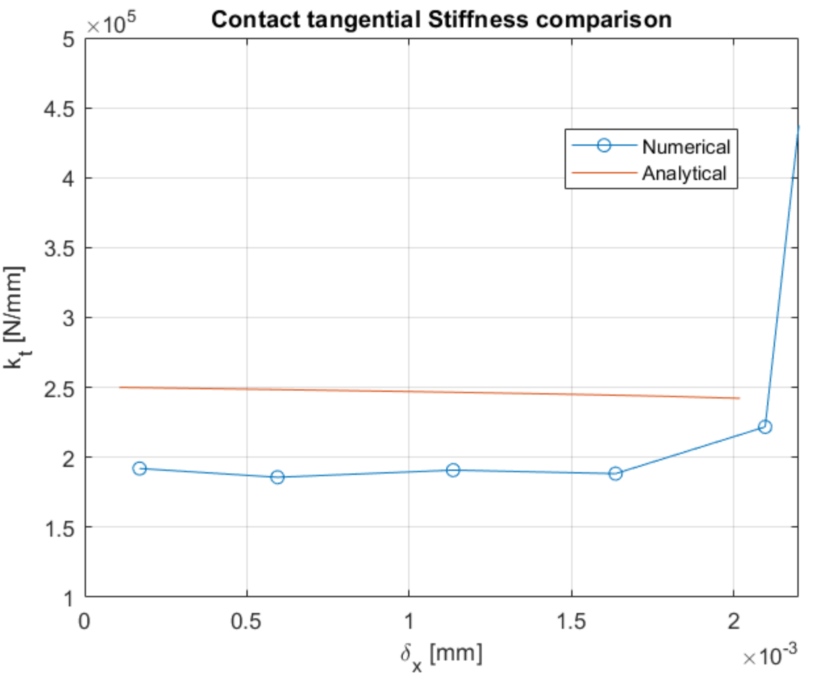

Figure 7.8: Contact tangential stiffness vs relative displacement comparison.

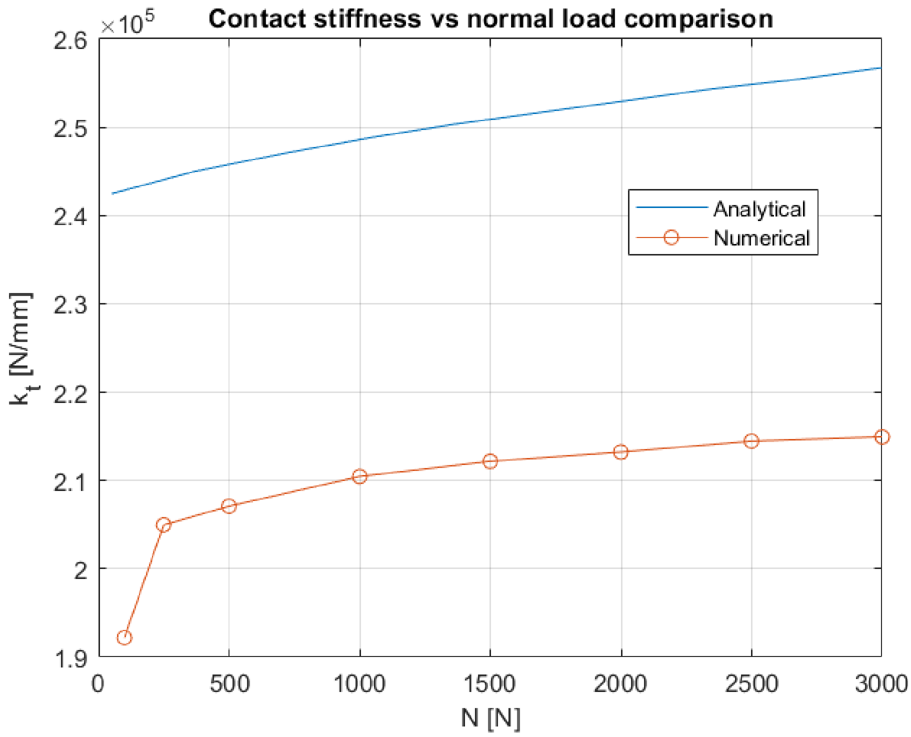

Figure 7.9: Contact tangential stiffness vs normal load comparison.

Chapter 8

Conclusions

Now that both analytical and numerical handlings are concluded, it is appropriate to draw some considerations about the results and propose some future developments and insights to be done. The first thing to point out is that, while the theory is compliant to the numerical data for normal problem, it is not entirely true for the tangential one. Indeed, the effects of twisting moment due to Q and the crushing due to P are not considered in followed literature, while affecting the solution in not negligible way. Moreover, the obtained results are calculated on a 2D model an then smeared on a 3D body, which increases the uncertainty about the solution, both numerical and analytical. For example, the bi-dimensional model does not account for the edge effects, so the presented results could be accurate only for a middle plain, far from the edges of the punch. In order to verify the data acquired, it should be then appropriate to compare the numerical results to the equivalent experimental data. Once that a full matching is achieved by correcting the theoretical equations, it will be possible to build a complete analytical model, capable of predicting accurately the contact stiffness without employing huge computing resources.
Then, summarizing what stated, the future perspectives of development for the described problem are the following:

- Build a new theoretical 2D model, capable of capturing the problem perturbations.
- Run the FE simulation for a 3D model and compare the results with the bi-dimensional output.
- Confront the numerical results with experimental data and correct the analytical model.

Bibliography

[1] D. Botto, M. Lavella, A numerical method to solve the normal and tangential contact problem of elastic bodies, *Wear* 330-331 (2015) 629-635.

[2] R.D. Mindlin, H. Deresiewicz, Elastic spheres in contact under varying oblique forces, *Journal of Applied Mechanics* 24 (1957) 623-624.

[3] R.D. Mindlin, Compliance of elastic bodies in contact, *Journal of Applied Mechanics* 16 (1949) 259-268.

[4] M. Ciavarella, G. Demelio, A review of analytical aspects of fretting fatigue, with extension to damage parameters, and application to dovetail joints, *International Journal of Solids and Structures* 38 (2001) 1791-1811.

[5] M. Ciavarella, D.A. Hills, G. Monno, The influence of rounded edges on indentation by flat punch, *Proceedings of the Institution of Mechanical Engineers* 212 (1998) 319–328.

[6] M. Allara, A model for characterization of friction contacts in turbine blades, *Journal of Sound and Vibration* 320 (2009) 527–544.

[7] D.A. Hills, D.Nowell, A. Sackfield, *Mechanics of Elastic Contacts*, Butterworth-Heinemann, Oxford, 1993.

[8] D.J. Segalman, M.J. Starr, Inversion of Masing models via continuous Iwan systems, *Non Linear Mechanics* 43 (2008) 74-80.

[9] https://www.sharcnet.ca